Transduction channels' gating can control friction on vibrating hair-cell bundles in the ear

Volker Bormuth[a,b,c], Jérémie Barral[a,b,c,1], Jean-François Joanny[a,b,c,d], Frank Jülicher[e], and Pascal Martin[a,b,c,2]

[a]Laboratoire Physico-Chimie Curie, Centre National de la Recherche Scientifique, Unité Mixte de Recherche 168, F-75248 Paris, France; [b]Institut Curie, Centre de recherche, F-75248 Paris, France; [c]Université Pierre et Marie Curie, F-75252 Paris, France; [d]École Supérieure de Physique et de Chimie Industrielles Paris Tech, F-75231 Paris, France; and [e]Max Planck Institute for the Physics of Complex Systems, D-01187 Dresden, Germany

Edited by David A. Weitz, Harvard University, Cambridge, MA, and approved April 8, 2014 (received for review February 12, 2014)

APPLIED PHYSICAL SCIENCES

BIOPHYSICS AND COMPUTATIONAL BIOLOGY

Hearing starts when sound-evoked mechanical vibrations of the hair-cell bundle activate mechanosensitive ion channels, giving birth to an electrical signal. As for any mechanical system, friction impedes movements of the hair bundle and thus constrains the sensitivity and frequency selectivity of auditory transduction. Friction is generally thought to result mainly from viscous drag by the surrounding fluid. We demonstrate here that the opening and closing of the transduction channels produce internal frictional forces that can dominate viscous drag on the micrometer-sized hair bundle. We characterized friction by analyzing hysteresis in the force–displacement relation of single hair-cell bundles in response to periodic triangular stimuli. For bundle velocities high enough to outrun adaptation, we found that frictional forces were maximal within the narrow region of deflections that elicited significant channel gating, plummeted upon application of a channel blocker, and displayed a sublinear growth for increasing bundle velocity. At low velocity, the slope of the relation between the frictional force and velocity was nearly fivefold larger than the hydrodynamic friction coefficient that was measured when the transduction machinery was decoupled from bundle motion by severing tip links. A theoretical analysis reveals that channel friction arises from coupling the dynamics of the conformational change associated with channel gating to tip-link tension. Varying channel properties affects friction, with faster channels producing smaller friction. We propose that this intrinsic source of friction may contribute to the process that sets the hair cell's characteristic frequency of responsiveness.

mechanosensitive channels | protein friction | hair-bundle mechanosensitivity | cell mechanics | auditory system

Sound evokes vibrations in the inner ear that are detected by sensory hair cells. Mechanosensitivity stems from mechanical activation of ion channels by tension changes in tip links that interconnect neighboring stereocilia of the hair-cell bundle (1). The acute sensitivity and sharp frequency selectivity of auditory detection rely on efficient transmission of the energy derived from the acoustic stimulus to the apparatus that mediates mechanoelectrical transduction. However, at least three sources of friction threaten to dissipate the energy of the vibrating hair bundle. First, viscous drag by the surrounding fluid provides a minimum source of damping (2, 3). Second, viscoelasticity of the tip links, or of proteins in series with these links, may result in additional dissipation during hair-bundle deflections (4). Third, an intrinsic source of friction—called "channel friction" in the following—is related to thermal fluctuations of the transduction channels between their open and closed states (5). The fluctuation–dissipation theorem dictates that this source of mechanical noise be related to friction forces on the hair bundle.

To circumvent the fundamental challenge posed by friction, hair cells mobilize internal energy resources to produce mechanical work, negate friction, and in turn amplify its inputs at a characteristic frequency (6, 7). In particular, the hair cell can power active movements of its hair bundle, including spontaneous oscillations (8, 9). Nevertheless, the performance of the hair bundle, both as transducer and amplifier, are influenced by friction for two reasons. First, friction limits the sensitivity of the hair bundle to weak inputs (5, 10). Second, the strength and dynamics of active force production must be tuned to balance friction that impedes movements of a particular bundle at its characteristic frequency (11). Despite their key role in hair-cell mechanosensitivity, the various sources of friction acting on a moving hair bundle, and how they depend on bundle velocity, have not been assayed directly through force measurements.

In this work, we combine a dynamic force assay with pharmacological tools to decipher the relative contributions of viscous drag, tip-link viscoelasticity, and channel friction to hair-bundle friction. By using a channel blocker to test the implication of transduction channels' gating, we unveil the contribution of channel friction. By disrupting the tip links, we decouple the transduction apparatus from bundle motion and measure viscous drag on the hair-bundle structure. We find that channel friction can dominate viscous drag. We also vary bundle velocity both to study the dynamical properties of friction and to determine how active hair-bundle motility affects friction estimates. We interpret our observations by developing a physical description of active hair-bundle mechanics and explain the mechanism of channel friction.

Results

To probe friction, we used flexible glass fibers to apply periodic stimuli to single hair-cell bundles from an excised preparation of the bullfrog's saccule (Fig. 1; *Materials and Methods*). Under natural ionic conditions, the hair bundles displayed spontaneous oscillations at frequencies of 5–80 Hz (12). We monitored the

Significance

In this work, we developed a dynamic force assay to characterize frictional forces that impede sound-evoked vibrations of hair-cell bundles, the mechanosensory antennas of the inner ear. We find that opening and closing of mechanosensitive ion channels in the hair bundle produce frictional forces that can dominate viscous drag on the hair-bundle structure. We show that channel friction can be understood quantitatively using a physical theory of hair-bundle mechanics that includes channel kinetics. Friction originating from gating of ion channels is a concept that is relevant to all mechanosensitive channels. In the context of hearing, this channel friction may contribute to setting the characteristic frequency of the hair cell.

Author contributions: V.B., J.B., J.-F.J., F.J., and P.M. designed research, performed research, analyzed data, and wrote the paper.

The authors declare no conflict of interest.

This article is a PNAS Direct Submission.

[1]Present address: Center for Neural Science, New York University, New York, NY 10003.

[2]To whom correspondence should be addressed. E-mail: pascal.martin@curie.fr.

This article contains supporting information online at www.pnas.org/lookup/suppl/doi:10.1073/pnas.1402556111/-/DCSupplemental.

www.pnas.org/cgi/doi/10.1073/pnas.1402556111

PNAS | **May 20, 2014** | vol. 111 | no. 20 | **7185–7190**

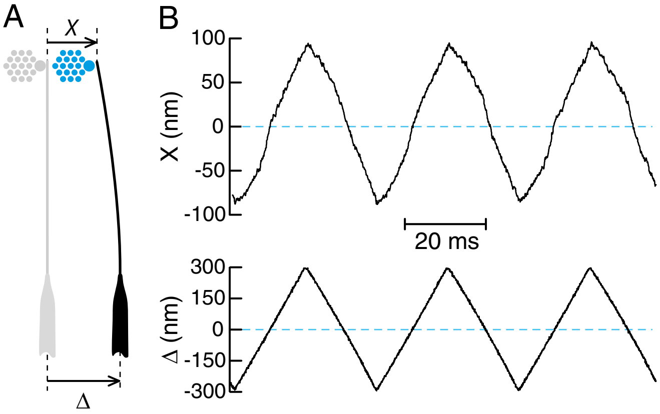

Fig. 1. Periodic triangular stimulation of a hair bundle. (*A*) Schematic top view of the experiment. The tip of a flexible fiber (black) is attached to the top of a hair bundle (blue). (*B*) Hair-bundle deflection X as a function of time (*Top*) in response to three cycles of a symmetric triangular movement Δ of the fiber's base (*Bottom*). Each positive or negative ramp of base motion had here a velocity of 34 $\mu m \cdot s^{-1}$; the bundle was subjected to a total of 71 cycles. The fiber had a stiffness $k = 295\ \mu N \cdot m^{-1}$ and a drag coefficient $\lambda = 113.4\ nN \cdot s \cdot m^{-1}$.

time-dependent position $X(t)$ of the fiber's tip, and thus of the attached hair bundle, in response to a symmetric triangular waveform of motion of the fiber's base. By convention, a movement of the hair bundle from negative to positive deflections increased tip-link tension and thus promoted channel opening. This positive half-cycle of stimulation was followed by a movement of opposite directionality that favored channel closure and completed the cycle. Because we fully characterized the mechanical and dynamical properties of the stimulus fiber (*SI Appendix*, section 2), we could compute, at each instant t, the force $F(t)$ that was applied by the fiber to the bundle. At each bundle position, the force exerted during the positive half-cycle of stimulation differed from that measured on the way back, causing hysteresis in the force–displacement relation (Fig. 2*A*).

Clockwise circulation around the hysteretic cycle reflects energy dissipation. We characterized the underlying frictional force by measuring the half-height of the hysteretic cycle

$$\Phi(X) = [F^{+}(X) - F^{-}(X)]/2 \qquad \textbf{[1]}$$

as a function of position. Here and in the following, signs in the superscripts indicate the directionality of bundle motion. For a passive system, the force Φ represents the arithmetic mean of the absolute frictional force on the positive and negative half-cycles at the same position X (*SI Appendix*, section 3). We note that active force production by the hair bundle can affect the width of the hysteretic cycle and thus contribute to Φ. The contribution of the active process, however, ought to become negligible when the period of stimulation gets significantly shorter than that of spontaneous hair-bundle oscillation. Interestingly, the force $F^{+}(X)$ and $F^{-}(X)$ displayed inversion symmetry with respect to a specific reference point at position $X_0 \cong 0$ (*SI Appendix*, Fig. S1). As a result, for stimuli faster than the internal active process, the force $\Phi(X = X_0)$ represents the true frictional force at this position.

The friction estimate Φ depended on bundle position (Fig. 2*B*, black curve). The relation $\Phi(X)$ was bell-shaped, with a peak centered near the position of inversion symmetry of the hysteretic cycle. Bundle velocity also varied with bundle position (Fig. 1*B* and *SI Appendix*, Fig. S2). On each half-cycle, this property was associated with a nonlinear region of reduced slope in the force–displacement relation, indicating that the hair bundle became transiently softer as it traversed this region (Fig. 2 *A* and *C*). Correspondingly, the bundle moved at increased velocity at these positions. However, a peak prevailed (Fig. 2*D*) when the frictional force was divided, at each position, by the average local velocity of the hair bundle (*SI Appendix*, Fig. S2). Hence, hair-bundle friction cannot be explained by viscous drag on a rigid object moving through the fluid.

Notably, friction peaked within the range of positions that spanned the regions of reduced slope of the force–displacement cycle. We recognized in hair-bundle softening the phenomenon of gating compliance (13), which here betrayed opening or closing of the mechanosensory channels that mediate mechanoelectrical transduction. In addition, the friction peak was associated with a shift—hereafter called the gating shift—between the positions of maximal gating compliance (Fig. 2 *A* and *C*): the channels opened at a position of the hair bundle that was more positive on the positive half-cycle than that at which they reclosed on the way back. These observations suggest that gating of the transduction channels was involved in the production of frictional forces.

To test this hypothesis, we used iontophoresis to apply gentamicin, an aminoglycoside antibiotic that blocks the transduction channels. As expected from complete blockage of the channels, there was no sign of gating compliance in the force–displacement relation (Fig. 2 *A* and *C*, red curve). Strikingly, the friction peak collapsed upon application of the drug (Fig. 2 *B* and *D*). The hysteretic cycle exhibited a nearly uniform width close to that

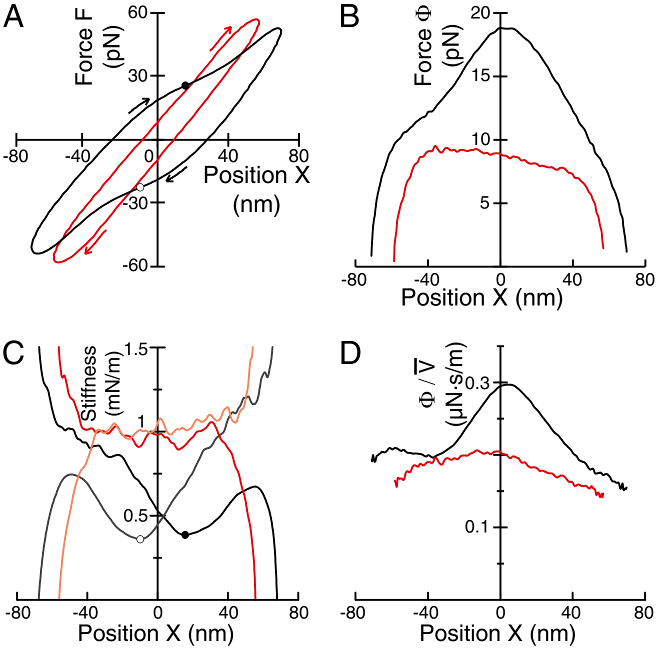

Fig. 2. Effects of a channel blocker on friction and stiffness. Black and red colors correspond, respectively, to measurements under control conditions and in the presence of a channel blocker. (*A*) External force F as a function of bundle position X. Arrows indicate clockwise circulation around a hysteretic cycle. The positions of minimal slope on the positive and negative half-cycles (black and white disk, respectively) are shifted by $\Delta X = +26$ nm. (*B*) Vertical half-height Φ of the hysteretic cycles shown in *A* as a function of bundle position X. (*C*) Hair-bundle stiffness, measured as the local slope of the curves shown in *A*, as a function of bundle position X for positive (dark colors) and negative (light colors) half-cycles of stimulation. (*D*) At each position X, the force Φ shown in *B* was divided by the arithmetic mean $\overline{V} = [|V^{+}(X)| + |V^{-}(X)|]/2$ of the absolute velocities that the hair bundle assumed on the positive and negative half-cycles when crossing this position. The ratio $\Phi/\overline{V}$ is plotted as a function of X. The velocity of the fiber's base was fixed at 200 $\mu m \cdot s^{-1}$; the hair bundle moved at a velocity $\overline{V} = 68\ \mu m \cdot s^{-1}$.

measured at large deflections under control conditions. We conclude that gating of the transduction channels evokes frictional forces on the hair bundle.

We then varied the velocity of stimulation. At low velocity of the fiber's base, we observed a counterclockwise circulation around the force–displacement cycle (*SI Appendix*, Fig. S3). This behavior reflects the work performed by an active process to power spontaneous oscillations of the hair bundle (14). Increasing the velocity switched the polarity of the hysteresis cycle, resulting in net positive dissipation (Fig. 3). We observed a dilation of the cycle along the force axis, with a more pronounced effect within the regions of gating compliance (Fig. 3*A*). Correspondingly, we measured negative frictional forces at low velocity, and a positive peak of friction emerged in response to increasing stimulus velocity (Fig. 3*B*).

If hydrodynamic drag were the dominant source of dissipation, we would expect friction to grow in proportion to velocity. A proportional growth was observed when the transduction machinery was decoupled from bundle motion by severing the tip links (Fig. 3*C* and *SI Appendix*, Fig. S4). Under this condition, the slope of the force–velocity relation provided a friction coefficient $\lambda_H = 86 \pm 29$ nN·s·m^{-1} (mean ± SD; n = 10). This value agrees with an estimate of the hydrodynamic drag coefficient of the hair bundle that resulted from finite-element simulations of the detailed interaction between the stereovillar structure and the fluid (2). Thus, friction on a bundle with severed tip links appears to be set by viscous drag.

With a fully functional transduction machinery, friction at the peak of the relation $\Phi(X)$ (Fig. 3*B*) displayed a sublinear growth with velocity (Fig. 3*C*). This behavior contrasts with the linear increase expected for hydrodynamic friction. At velocities larger than ~20 μm·s^{-1}, friction on the intact bundle was larger than that measured with broken tip links. The hair bundle thus appeared to be subjected to an intrinsic source of friction that adds to viscous drag. We then estimated friction within the shoulders of the friction peak (Fig. 3 *B* and *C*). After a steep rise at low velocities, friction matched that observed when the channels were blocked. This congruence makes sense because the stimulus ought to elicit no significant channel gating at the edges of the hysteretic cycle, where the channels are expected to be either mostly closed or open. As velocity increased, the two force–velocity relations approached the linear relation that was measured with severed tip links. However, friction was larger with channels blocked than with severed tip links, indicating that viscous drag was supplemented by additional friction even in the case where the channels were unable to gate.

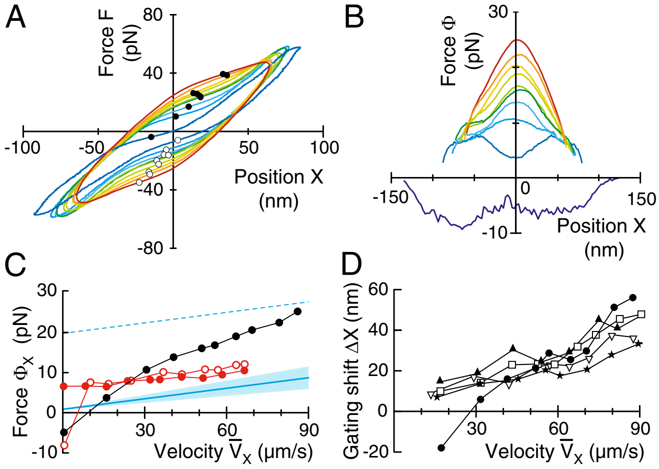

Fig. 3. Effects of stimulus velocity. (*A*) Force–displacement relations for increasing velocities of triangular stimulation (blue to red; cycle at lowest velocity shown in *SI Appendix*, Fig. S3). Positions of maximal gating compliance are marked by black and white disks (positive and negative half-cycle, respectively). (*B*) Friction estimate Φ as a function of bundle position *X*. (*C*) Under control conditions (same data as in *A* and *B*), the force Φ at $X = 3.5$ nm (black disks) or at $X = -52$ nm (red circles), noted Φ_X, is plotted as a function of the mean bundle velocity at this position, $\overline{V}_X$. Friction was also estimated in the presence of a channel blocker (red disks; same cell) and after severing the tip links (cyan solid line: mean behavior of 10 other cells; edges of the shaded region: SDs to the mean slope). The dashed line (same slope as the cyan solid line) serves as a guideline for the asymptotic behavior expected for the relation $\Phi_X(\overline{V}_X)$ under control conditions (Fig. 4*E*). (*D*) Gating shift Δ*X* as a function of velocity $\overline{V}_X$ at the peak of $\Phi(X)$ for five different cells, including that used in *A*–*C* (black disks).

Finally, we observed that the gating shift increased with bundle velocity (Fig. 3 *A* and *D*). This property reveals that the larger the velocity of motion, the further that bundle had to move in each direction before the transduction channels would actually gate. For velocities larger than ~30 μm·s^{-1}, the gating shift increased approximately in proportion to velocity. The slope of this relation provides twice the time of channel gating, which, at these velocities, is $\tau_{exp} = 230 \pm 40$ μs (mean ± SD; n = 5). This value lies within the range of the activation time constants of the transduction currents that were measured with the same type of hair cells (15). We reasoned that when the bundle moves, extra elastic energy is stored in the gating springs during the typical time τ_{exp} before the channels gate. Upon channel gating, this extra energy should be dissipated, giving rise to friction (16). In turn, we hypothesized that the friction peak that we observed in our recordings (Fig. 3*B*) may constitute the mechanical signature of delayed channel gating.

To test this inference, we introduced finite activation kinetics of the transduction channels into a physical description of active hair-bundle mechanics (17). First ignoring viscous drag and the active process, we studied the consequences of delayed gating for a passive bundle (*SI Appendix*, section 4). In response to triangular stimulation, the force–displacement relation shows hysteresis (Fig. 4*A*). Although no explicit source of dissipation was included in the description, we find that the system is subjected to frictional forces. Thus, delayed channel gating produces friction. As in our experiments (Fig. 2*B*), the mean frictional force Φ depends on position and displays a maximum (Fig. 4*B*). The theory indicates that this force is maximal at the position where the channels are half-open at steady state. When estimated at the peak, channel friction displays a sublinear growth as a function of velocity until it saturates to $\Phi_{max} = NZ/2$ at large velocities. Here N is the number of transduction channels operating in parallel within a hair bundle, and Z—the gating force (13)—represents the reduction in tip-link tension upon the conformational change associated with channel opening. At low velocities, the frictional force varies in proportion to velocity with a friction coefficient

$$\lambda_C = NZ^2\tau/(4k_BT). \quad [2]$$

Its value depends on the characteristic timescale τ of channel activation. Channel friction vanishes with instantaneous channel gating ($\tau \to 0$). In addition, channel-gating kinetics introduces a shift between the positions of channel opening and closing within the stimulation cycle. Simulations indicate that τ can be obtained from half the initial slope of the relation between the gating shift and velocity (Fig. 4*F*). With parameters listed in *SI Appendix*, Table S1, we find $\lambda_C = 1$ μN·s·m$^{-1} \cong 10 \times \lambda_H$. These values indicate that friction owing to gating of the transduction channels can indeed be strong enough to dominate viscous drag on the hair-bundle structure.

Because the hair bundle displays active motility (*SI Appendix*, Fig. S3), the force Φ is expected to depart from the passive friction estimate discussed in the preceding paragraph. To determine

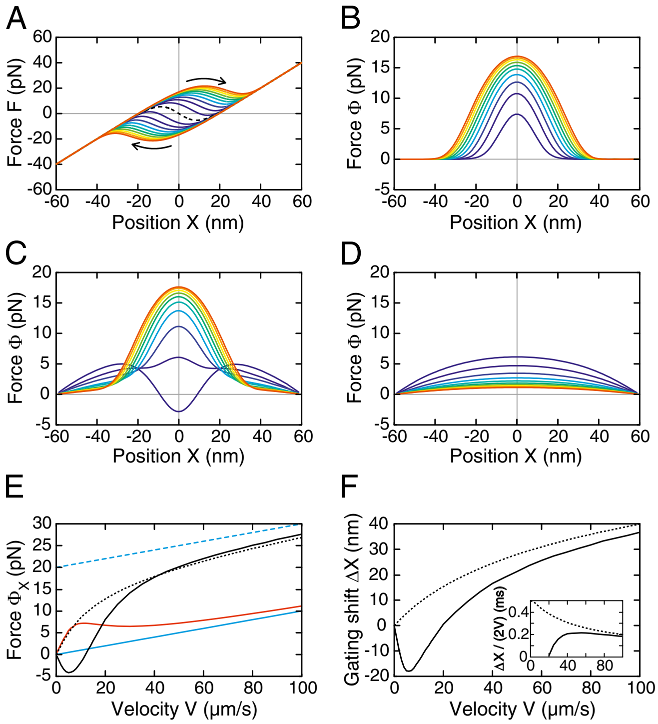

Fig. 4. Simulations of hair-bundle mechanics. The hair bundle follows triangular waveforms of motion. In *A*–*D*, viscous drag is ignored; bundle velocity V increases from 10 $\mu m \cdot s^{-1}$ (dark blue) to 100 $\mu m \cdot s^{-1}$ (red) in nine 10-$\mu m \cdot s^{-1}$ steps. (*A*) Force–displacement cycles $F(X)$ for a passive bundle (no adaptation). Arrows indicate clockwise circulation. With instantaneous channel gating, hysteresis vanishes (dashed line). (*B*) Channel-friction force Φ as a function of position X for the hysteretic cycles shown in *A*. (*C*) Relation $\Phi(X)$ with functional transduction channels and adaptation. (*D*) Relation $\Phi(X)$ resulting from adaptation when the channels are blocked. (*E*) Force Φ at $X = 0$, noted Φ_X, as a function of bundle velocity V when dissipation comes from viscous drag only (cyan solid), from channel friction and viscous drag (black dotted), from channel friction, viscous drag and adaptation (black solid), and from viscous drag and adaptation when the channels are blocked (red). At larges velocities, the relation $\Phi_X(V)$ (black solid and dotted) shows an asymptotic linear behavior (dashed cyan). (*F*) Gating shift ΔX, and estimate $\Delta X/(2V)$ of the channel activation time (*Inset*), as a function of bundle velocity V with or without adaptation (solid and dotted lines, respectively). Parameters in *SI Appendix*, Table S1.

how active hair-bundle motility affects Φ, we included calcium-dependent adaptation of the transduction apparatus (17) to our description (*SI Appendix*, section 5). At the edges of the stimulation cycle, where the channels are nearly all open or closed and thus do not add extra friction, or equivalently when the channels are blocked, adaptation produces in our simulations a positive contribution to the force Φ that leads to an overestimate of frictional forces (Fig. 4 *C*–*E*). This behavior may explain why the measured friction was larger with channels blocked than when the tip links were severed (Fig. 3*C*), although the tip links may by themselves be viscoelastic (4) or engage dissipative relative movements of adjacent stereocilia (18). In contrast, in the region of channel gating, the theory shows that frictional forces are underestimated at low bundle velocities, for the active process provides a negative contribution to Φ (Fig. 4 *C* and *E*). The effect of the active process can be neglected when the stimulus becomes fast enough to outrun adaptation but is significant at low velocities, where Φ can become negative (Fig. 4*E*). In the case where adaptation is functional (black solid line in Fig. 4*E*), we can construct a line of positive slope that starts from the origin and touches the force–velocity relation in one point. Its slope λ_0 provides a lower bound to the drag coefficient $\lambda_H + \lambda_C$ resulting from viscous drag and channel friction. In experiments (Fig. 3*C*), we measured a value $\lambda_0 = 425 \pm 70$ $nN \cdot s \cdot m^{-1}$ (mean ± SD; $n = 6$), which was nearly fivefold the hydrodynamic drag coefficient λ_H. In addition, at velocities larger than 40 $\mu m \cdot s^{-1}$, where the active process can be neglected, the slope of the relation between the gating shift and velocity (Figs. 3*D* and 4*F*) accounts for our measurement of the channel time $\tau_{exp} \cong 230$ μs (Fig. 4*F*, *Inset*).

Discussion

Physical Origin of Channel Friction. Our results demonstrate that gating of the transduction channels provides a major contribution to hair-bundle friction. It is striking that a few tens of ion channels (19, 20) can have a significant effect on friction of a structure as large as the micrometer-sized hair-cell bundle. If channel friction resulted simply from viscous drag associated with conformational changes of the channels moving in a fluid, we would estimate a friction coefficient ξ_H that is nearly four orders of magnitude lower than the value $\lambda_C \cong 340$ $nN \cdot s \cdot m^{-1}$ measured here at low bundle velocity (*SI Appendix*, section 4).

Our physical description of hair-bundle mechanics attributes high channel friction to an intrinsic source of dissipation associated with channel gating (Fig. 4 and *SI Appendix*, section 4). In a simplified view, this can be explained by introducing an energy barrier E_a between two conformations of a channel. The effective friction coefficient associated to channel gating can then be approximated by $\xi \times \exp[E_a/(k_B T)]$, where ξ represents a microscopic friction coefficient acting on the channels' gates (21). If we take for ξ the rough hydrodynamic estimate ξ_H given above, an energy barrier $E_a \cong 10$ $k_B T$ (15) brings channel friction to a level compatible with our experiments. Internal friction resulting from barrier crossing is thought to influence many processes in biology, including protein folding (22), protein–protein interactions (23, 24), cell adhesion (25), and the speed and efficiency of motor proteins (16, 26). Our work shows that this general concept of barrier friction also applies to mechanosensory ion channels and is thus relevant for the detection of sound-evoked vibrations by hair-cell bundles in the ear.

In the hair bundle, mechanosensitivity relies on strong coupling between the gating dynamics of the transduction channels and tip-link tension. If a change in tip-link tension affects the open probability of a transduction channel, then, reciprocally, channel gating must impinge on tip-link tension and thus produce force on the hair bundle (13, 27). However, it takes time to break the bonds that maintain an ion channel in a closed state. Channel-gating forces in turn lag the stimulus, which results in frictional resistance to hair-bundle movements and mechanical hysteresis. The effect of channel friction on the hair bundle is thus intimately related to the function of this organelle as a mechanoreceptor (*SI Appendix*, section 4).

Dual Role of Channel-Gating Forces. Sensitive mechanotransduction by hair cells calls for minimal frictional resistance to hair-bundle vibrations. However, our findings suggest that the hair bundle is not optimized to keep friction at the minimum level set by viscous drag on the hair-bundle structure. Weaker gating forces would reduce channel friction (Eq. 2 and *SI Appendix*, section 4). However, decreasing the magnitude of the gating force also broadens the sigmoidal relation between the channels' open probability and bundle displacement at thermal equilibrium (*SI Appendix*, section 4, Eq. S42) (28). Larger bundle displacements would in turn be required to elicit significant transduction currents, corresponding to lower mechanosensitivity of the transducer. Moreover, large gating forces also promote negative stiffness of the hair bundle, a property that has been shown to be instrumental in an active process that counteracts friction and in turn amplifies weak stimuli (29–31). Thus, gating forces may underlie both a prominent source of hair-bundle friction and part of the solution to the general problem posed by friction to bundle mechanosensitivity.

Effect of Channel Friction on Characteristic Frequency. Frequency selectivity is a hallmark of active mechanosensation by hair cells. Several mechanisms have been implicated in the process that sets the characteristic frequency of optimal responsiveness, including electrical tuning of receptor potentials and passive mechanical resonance in a spring-mass system associated to accessory structures (32). Notably, spontaneous hair-bundle oscillations also provide a characteristic frequency near which the cell resonates with sinusoidal inputs, thus operating as an active filter (33). The active mechanical resonance occurs near the frequency of the periodic stimulus where active hair-bundle motility cancels friction (30, 34), which in our experiments happens at ∼10 Hz (Fig. 3*C*). This characteristic frequency is more than a hundredfold smaller than the inverse of the channel activation time (>1 kHz). Consequently, the hair bundle operates in the low-frequency regime of channel friction, where this source of friction dominates viscous drag (Fig. 4 and *SI Appendix*, Fig. S10 in section 4). The characteristic frequency of the active resonator is expected to decrease with the frictional load (35, 36). The characteristic frequency should thus depend on the number of the transduction channels, the value of their gating force, and of their activation time (Eq. 2). In particular, faster channels ought to produce smaller channel friction, which would then allow faster hair-bundle movements. This property may be relevant to auditory organs where the activation kinetics of the transduction channels (37, 38), as well as the number and height of the stereocilia (39, 40), has been shown to vary systematically along a tonotopic axis. Varying channel properties, and in turn channel friction, could in principle help the hair cells set their characteristic frequency of maximal mechanical responsiveness over the broad range required for the analysis of complex natural sounds.

Auditory hair cells, in particular in the mammalian cochlea, are endowed with much faster channels than those of the low-frequency hair cells that we studied here in the bullfrog's sacculus. For instance, outer hair cells within the apical turn of the rat cochlea display activation channel times $\tau_{rat} \leq 50$ µs (37, 41). Although these cells respond to relatively high frequencies of ∼4 kHz, their characteristic frequency remains significantly smaller than the inverse of the channel time (>20 kHz). Auditory hair cells can thus operate in the low-frequency regime of channel friction. One may wonder whether channel friction is large enough to be relevant at auditory frequencies, for the magnitude of channel friction is expected to decrease with faster channels (Eq. 2). However, the number of channels that contribute to channel friction is larger for high-frequency than for low-frequency cells. In addition, the bundle height is smaller at high frequencies, which magnifies the effect of channel-gating forces (*SI Appendix*, section 4.3). Using scaling arguments, we estimate frictional forces from channel gating that may again be larger than those resulting from viscous drag (*SI Appendix*, section 4.3). Although experiments are needed to test this prediction, our results raise the possibility that channel friction may contribute to the complex process that sets the characteristic frequency of an auditory hair cell.

Materials and Methods

Experimental Preparation. Details of the experimental procedure have been published elsewhere (17). Briefly, an excised preparation of the bullfrog's (Rana catesbeiana) saccule was mounted on a two-compartment chamber. The basal bodies of hair cells were bathed in standard saline containing (in mM): 110 NaCl, 2 KCl, 4 $CaCl_2$, 3 D-glucose, 2 Na_2-creatine phosphate, 2 Na-pyruvate, and 5 Na-Hepes. Hair bundles instead projected into an artificial endolymph of composition (in mM): 2 NaCl, 118 KCl, 0.25 $CaCl_2$, 3 D-glucose, and 5 Na-Hepes. To disconnect the hair bundles from the overlying otolithic membrane, the apical surface of the preparation was exposed for 20–30 min to endolymph supplemented with 50–67 mg·mL^{-1} of the protease subtilisin (type XXIV or VIII, Sigma). The otolithic membrane was then peeled off to obtain access to individual hair bundles. Experiments were performed at room temperature.

Microscopic Apparatus and Mechanical Stimulation. The preparation was viewed through a 60× water-immersion objective of an upright microscope (BX51WI, Olympus). The tip of a stimulus fiber was affixed to the kinociliary bulb of an individual hair bundle and imaged at a magnification of 1000× onto a displacement monitor that included a dual photodiode. Calibration was performed by measuring the output voltages of the monitor in response to a series of offset displacements of the photodiode. For movements of the fiber's tip that did not exceed ±150 nm in the sample plane, the displacement monitor was linear. Stimulus fibers were fabricated from borosilicate capillaries and coated with a thin layer of gold-palladium to enhance contrast.

The fiber was secured by its base to a stack-type piezoelectric actuator (PA-8/14, Piezosystem Jena) driven by a custom-made power supply (Elbatech). The voltage command to the actuator was a symmetric triangle wave that imposed back-and-forth movements of the fiber's base with a peak-to-peak magnitude of 600 nm. Except during the ∼1 ms that it took to reverse the directionality of motion at the end of each half-cycle, the absolute velocity of the base was nearly fixed (*SI Appendix*, Fig. S2). In a typical run, this velocity was increased sequentially from 1 to 300 µm·s^{-1} in nine steps. The fundamental frequency of the stimulus thus varied from 0.8 to 250 Hz, corresponding to a period of stimulation that decreased from 1.2 s to 4 ms. The slowest stimulus was maintained for four cycles. At higher frequencies, the stimulus lasted 2.4 s, corresponding to tens-to-hundreds of cycles of stimulation at each frequency. Because piezoelectric actuators display hysteresis, their movements do not precisely reflect the command signal. The actual movement of the fiber's base was thus recorded with the displacement monitor at a magnification of 294×; the measurement was performed before or after hair-bundle stimulation. Base and tip positions of the fiber were thus measured with the same acquisition line, which ensured that no delay was artificially introduced between the two positions by the recording procedure. Any delay would be erroneously interpreted as friction in our estimates of the external force applied to the hair bundle by the fiber.

Fiber Calibration and Force Determination. We characterized the mechanical properties of a fiber immersed in endolymph by analyzing the Brownian motion of the free fiber's tip while the base was clamped at a fixed position (*SI Appendix*, section 2.3). The power spectrum of fluctuations was fitted by a Lorentzian, which provided a stiffness k = 200–500 µN·m^{-1} and a drag coefficient λ = 80–140 nN·s·m^{-1}. As far as fluctuations were concerned, the fiber thus behaved as a first-order low-pass filter with an angular cutoff frequency $\omega_1 = k/\lambda = 1.5 - 5.5 \times 10^3$ rad·s^{-1}.

For each triangle wave of stimulation, we computed the mean cycle of the fiber's tip $X(t)$ and base $\Delta(t)$ positions as a function of time t by performing ensemble averages over all cycles of the corresponding waveforms. We then computed the first 30 Fourier components of the average cycles. For the fiber's base, they are given by $\tilde{\Delta}_n = (2/T)\int_0^T \Delta(t)\, e^{+i\,n\,\omega_0\,t} dt$ for $1 \leq n \leq 30$ and $\tilde{\Delta}_0 = \langle \Delta(t) \rangle$ where $T = 2\pi/\omega_0$ is the period of the stimulus and $i^2 = -1$. Similar relations can be written for the Fourier components $\tilde{X}_n$ of tip motion. Assuming that the stimulus fiber behaves as a slender rod, the force applied by the fiber's tip on the hair bundle was then calculated as (*SI Appendix*, section 2)

$$F(t) = \mathrm{Re}\left(\sum_{n=0}^{30} \left[\tilde{F}_n\, e^{-i\,n\,\omega_0\,t} \right] \right), \qquad [3]$$

in which the n^{th} Fourier component of the force is given by

$$\tilde{F}_n = \frac{4}{\beta_1^4} k\ \alpha_n^3 \left[\frac{1 + \cos\alpha_n \times \cosh\alpha_n}{\cos\alpha_n \times \sinh\alpha_n - \sin\alpha_n \times \cosh\alpha_n} \tilde{X}_n - \frac{\cos\alpha_n + \cosh\alpha_n}{\cos\alpha_n \times \sinh\alpha_n - \sin\alpha_n \times \cosh\alpha_n} \tilde{\Delta}_n \right]. \qquad [4]$$

Here we introduced the frequency-dependent parameter $\alpha_n^4 = i\,n\,\omega_0/\omega_S$, with $\omega_S = \omega_1/\beta_1^4$, ω_1 the angular cutoff frequency of thermal fluctuations of the fiber's tip (see previous paragraph), and in which $\beta_1 \cong 1.8751$ is the smallest positive solution of $\cos\beta_1 \times \cosh\beta_1 = -1$. Data analysis was performed with Matlab (the Mathworks, version R2011b).

Iontophoresis of a Channel Blocker and of a Ca^{2+} Chelator. We used iontophoresis of gentamicin to reversibly block the transduction channels of a hair bundle (12). With the same technique, we also applied the chelator 1,2-bis(2-aminophenoxy)ethane-N,N,N′,N′-tetraacetic acid (BAPTA) to sever the tip links by locally reducing the endolymphatic Ca^{2+} concentration. Coarse microelectrodes were fabricated from borosilicate capillaries with a pipette puller (P97, Sutter Instrument). The resistance of the electrodes was 10 MΩ when filled with 3 M KCl and immersed in the same solution. For the experiments the electrodes were filled with 500 mM gentamicin sulfate (G-4793, Sigma) or with 500 mM BAPTA (A4926, Sigma). These compounds were each dissolved in an aqueous solution containing 25 mM KCl. In each experiment, the electrode's tip was situated at ∼3 μm from the hair bundle. Under control conditions, a holding current was applied to counteract the diffusive release of ions from the electrode.

Signal Generation and Acquisition. All signals were generated and acquired under the control of a computer running a user interface programmed with LabVIEW software (version 2011; National Instruments). The command signal controlling the movement of the base of a stimulus fiber was produced by a 16-bit interface card at a sampling rate of 25 kHz (PCI-6733, National Instruments). A second interface card (PCI-6250, National Instruments) conducted signal acquisition with a precision of 16 bits and a sampling rate of 25 kHz. Signals coming from the displacement monitor or going to the stimulation apparatus were conditioned with an eight-pole Bessel antialiasing filter adjusted to a low-pass half-power frequency of 12.5 and 0.5 kHz, respectively.

ACKNOWLEDGMENTS. We thank Jonathon Howard, Thomas Risler, Erik Schäffer, and Mélanie Tobin for comments on the manuscript, and Benoît Lemaire and Rémy Fert from the machine shop of the Curie Institute. This work was supported by the French National Agency for Research (ANR-11-BSV5-0011). V.B. was supported by a long-term fellowship of the Federation of European Biochemical Societies. J.B. is alumnus of the Frontiers in Life Science PhD program of the University Paris Diderot and thanks the Fondation Pierre-Gilles de Gennes for a doctoral fellowship.

1. Gillespie PG, Müller U (2009) Mechanotransduction by hair cells: Models, molecules, and mechanisms. *Cell* 139(1):33–44.
2. Kozlov AS, Baumgart J, Risler T, Versteegh CP, Hudspeth AJ (2011) Forces between clustered stereocilia minimize friction in the ear on a subnanometre scale. *Nature* 474(7351):376–379.
3. Denk W, Webb WW, Hudspeth AJ (1989) Mechanical properties of sensory hair bundles are reflected in their Brownian motion measured with a laser differential interferometer. *Proc Natl Acad Sci USA* 86(14):5371–5375.
4. Kozlov AS, Andor-Ardó D, Hudspeth AJ (2012) Anomalous Brownian motion discloses viscoelasticity in the ear's mechanoelectrical-transduction apparatus. *Proc Natl Acad Sci USA* 109(8):2896–2901.
5. Nadrowski B, Martin P, Jülicher F (2004) Active hair-bundle motility harnesses noise to operate near an optimum of mechanosensitivity. *Proc Natl Acad Sci USA* 101(33): 12195–12200.
6. Hudspeth AJ (2008) Making an effort to listen: mechanical amplification in the ear. *Neuron* 59(4):530–545.
7. Ashmore J, et al. (2010) The remarkable cochlear amplifier. *Hear Res* 266(1–2):1–17.
8. Fettiplace R, Hackney CM (2006) The sensory and motor roles of auditory hair cells. *Nat Rev Neurosci* 7(1):19–29.
9. Barral J, Martin P (2011) The physical basis of active mechanosensitivity by the hair-cell bundle. *Curr Opin Otolaryngol Head Neck Surg* 19(5):369–375.
10. Barral J, Dierkes K, Lindner B, Jülicher F, Martin P (2010) Coupling a sensory hair-cell bundle to cyber clones enhances nonlinear amplification. *Proc Natl Acad Sci USA* 107(18):8079–8084.
11. Gummer AW, Hemmert W, Zenner HP (1996) Resonant tectorial membrane motion in the inner ear: its crucial role in frequency tuning. *Proc Natl Acad Sci USA* 93(16): 8727–8732.
12. Martin P, Bozovic D, Choe Y, Hudspeth AJ (2003) Spontaneous oscillation by hair bundles of the bullfrog's sacculus. *J Neurosci* 23(11):4533–4548.
13. Howard J, Hudspeth AJ (1988) Compliance of the hair bundle associated with gating of mechanoelectrical transduction channels in the bullfrog's saccular hair cell. *Neuron* 1(3):189–199.
14. Martin P, Hudspeth AJ (1999) Active hair-bundle movements can amplify a hair cell's response to oscillatory mechanical stimuli. *Proc Natl Acad Sci USA* 96(25):14306–14311.
15. Corey DP, Hudspeth AJ (1983) Kinetics of the receptor current in bullfrog saccular hair cells. *J Neurosci* 3(5):962–976.
16. Tawada K, Sekimoto K (1991) Protein friction exerted by motor enzymes through a weak-binding interaction. *J Theor Biol* 150(2):193–200.
17. Tinevez JY, Jülicher F, Martin P (2007) Unifying the various incarnations of active hair-bundle motility by the vertebrate hair cell. *Biophys J* 93(11):4053–4067.
18. Kozlov AS, Risler T, Hinterwirth AJ, Hudspeth AJ (2012) Relative stereociliary motion in a hair bundle opposes amplification at distortion frequencies. *J Physiol* 590(Pt 2): 301–308.
19. Holton T, Hudspeth AJ (1986) The transduction channel of hair cells from the bull-frog characterized by noise analysis. *J Physiol* 375(1):195–227.
20. Beurg M, Fettiplace R, Nam JH, Ricci AJ (2009) Localization of inner hair cell mechanotransducer channels using high-speed calcium imaging. *Nat Neurosci* 12(5):553–558.
21. de Gennes P-G (1979) *Scaling Concepts In Polymer Physics*. (Cornell Univ Press, Ithaca), pp 170, 198.
22. Ansari A, Jones CM, Henry ER, Hofrichter J, Eaton WA (1992) The role of solvent viscosity in the dynamics of protein conformational changes. *Science* 256(5065): 1796–1798.
23. Evans E (2001) Probing the relation between force—lifetime—and chemistry in single molecular bonds. *Annu Rev Biophys Biomol Struct* 30:105–128.
24. Braun M, et al. (2011) Adaptive braking by Ase1 prevents overlapping microtubules from sliding completely apart. *Nat Cell Biol* 13(10):1259–1264.
25. Evans EA, Calderwood DA (2007) Forces and bond dynamics in cell adhesion. *Science* 316(5828):1148–1153.
26. Bormuth V, Varga V, Howard J, Schäffer E (2009) Protein friction limits diffusive and directed movements of kinesin motors on microtubules. *Science* 325(5942):870–873.
27. van Netten SM, Kros CJ (2000) Gating energies and forces of the mammalian hair cell transducer channel and related hair bundle mechanics. *Proc Biol Sci* 267(1455): 1915–1923.
28. Markin VS, Hudspeth AJ (1995) Gating-spring models of mechanoelectrical transduction by hair cells of the internal ear. *Annu Rev Biophys Biomol Struct* 24:59–83.
29. Martin P, Mehta AD, Hudspeth AJ (2000) Negative hair-bundle stiffness betrays a mechanism for mechanical amplification by the hair cell. *Proc Natl Acad Sci USA* 97(22):12026–12031.
30. Martin P, Hudspeth AJ, Jülicher F (2001) Comparison of a hair bundle's spontaneous oscillations with its response to mechanical stimulation reveals the underlying active process. *Proc Natl Acad Sci USA* 98(25):14380–14385.
31. Nam JH, Fettiplace R (2008) Theoretical conditions for high-frequency hair-bundle oscillations in auditory hair cells. *Biophys J* 95(10):4948–4962.
32. Fettiplace R, Fuchs PA (1999) Mechanisms of hair cell tuning. *Annu Rev Physiol* 61: 809–834.
33. Martin P (2008) *Active Hair-Bundle Motility of the Hair Cells of Vestibular and Auditory Organs. Active Processes and Otoacoustic Emissions in Hearing, Springer Handbook of Auditory Research*, eds Manley GA, Popper AN, Fay RR (Springer, New York), pp 93–143.
34. Martin P, Hudspeth AJ (2001) Compressive nonlinearity in the hair bundle's active response to mechanical stimulation. *Proc Natl Acad Sci USA* 98(25):14386–14391.
35. Camalet S, Duke T, Jülicher F, Prost J (2000) Auditory sensitivity provided by self-tuned critical oscillations of hair cells. *Proc Natl Acad Sci USA* 97(7):3183–3188.
36. Duke T, Jülicher F (2008) *Critical Oscillators as Active Elements in Hearing. Active Processes and Otoacoustic Emissions, Springer Handbook of Auditory Research*, eds Manley GA, Popper AN, Fay RR (Springer, New York), pp 63–92.
37. Ricci AJ, Kennedy HJ, Crawford AC, Fettiplace R (2005) The transduction channel filter in auditory hair cells. *J Neurosci* 25(34):7831–7839.
38. Ricci A (2002) Differences in mechano-transducer channel kinetics underlie tonotopic distribution of fast adaptation in auditory hair cells. *J Neurophysiol* 87(4):1738–1748.
39. Lim DJ (1986) Functional structure of the organ of Corti: A review. *Hear Res* 22(1-3): 117–146.
40. Roth B, Bruns V (1992) Postnatal development of the rat organ of Corti. II. Hair cell receptors and their supporting elements. *Anat Embryol (Berl)* 185(6):571–581.
41. Kennedy HJ, Evans MG, Crawford AC, Fettiplace R (2003) Fast adaptation of mechanoelectrical transducer channels in mammalian cochlear hair cells. *Nat Neurosci* 6(8): 832–836.

SI Appendix for

Transduction channels' gating can control friction on vibrating hair-cell bundles in the ear

Volker Bormuth, Jérémie Barral, Jean-François Joanny, Frank Jülicher, Pascal Martin[1]

[1] *To whom correspondence should be addressed: Email: pascal.martin@curie.fr*

Contents

Section 1: **Supplementary data (Figs. S1-S4)**

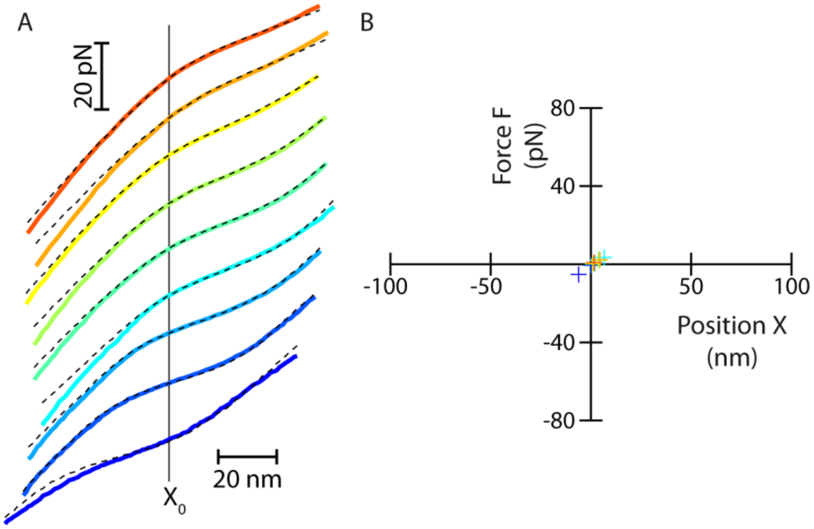

Fig. S1. Inversion symmetry of force-displacement relations. (A) *For each velocity of triangular stimulation but the lowest, we superimpose the force displacement relation* $F^{+}(X_0 + u) - F_0$ *for the positive half cycle (colors; increasing velocity from blue to red) on the relation* $-[F^{-}(X_0 - u) - F_0]$ *for the negative half cycle (black dashed lines). Here,* $u = X - X_0$ *and X is the hair-bundle position. In each case, the constant* X_0 *was obtained by finding the position of the local extremum near the origin in the relation* $\Phi(X)$ *(see Fig. 3B in the main text) and we set* $F_0 = [F^{+}(X_0) + F^{-}(X_0)]/2$*. Same data as those shown in Fig. 3 of the main text; the fourth trace from the top corresponds to the data shown in Fig. 2.* ***(B)*** *Plot of the points* (X_0, F_0) *that were used in A to apply the inversion-symmetry transformation to the force-displacement relations. The color code is the same as in A.*

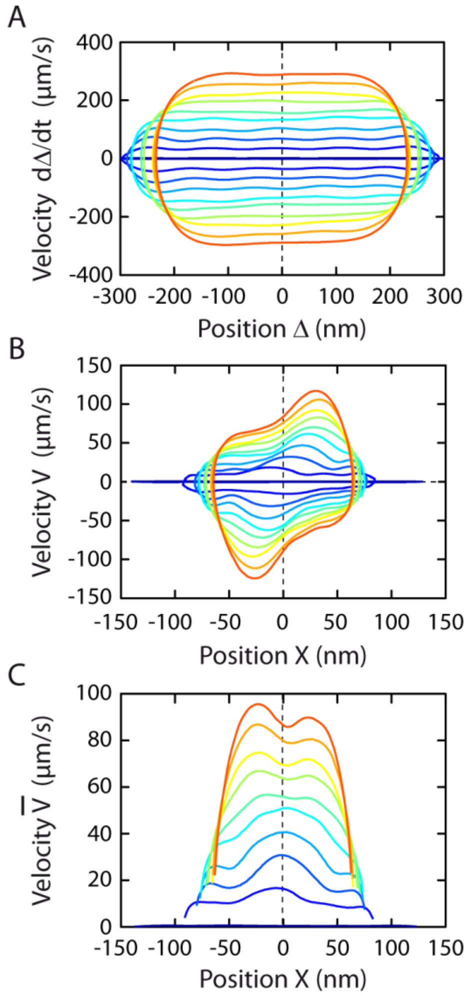

Fig. S2. Velocity of fiber and bundle movements. ***(A)*** *The velocity* $d\Delta/dt$ *of the fiber's base is plotted as a function of base position* Δ *for all 10 triangular waveforms of base motion.* ***(B)*** *The velocity* $V = dX/dt$ *of the fiber's tip, or equivalently of the hair bundle attached to it, is plotted as a function of tip position X. Tip movements resulted from the series of stimuli shown in A.* ***(C)*** *The arithmetic mean* $\bar{V} = [|V^{+}(X)| + |V^{-}(X)|]/2$ *of the absolute velocities of the fiber's tip is plotted as a function of the position X for the recordings shown in B. This data is associated to Figs. 1-3 of the main text, with the fourth trace from the top corresponding to the data shown in Fig 2 (control conditions).*

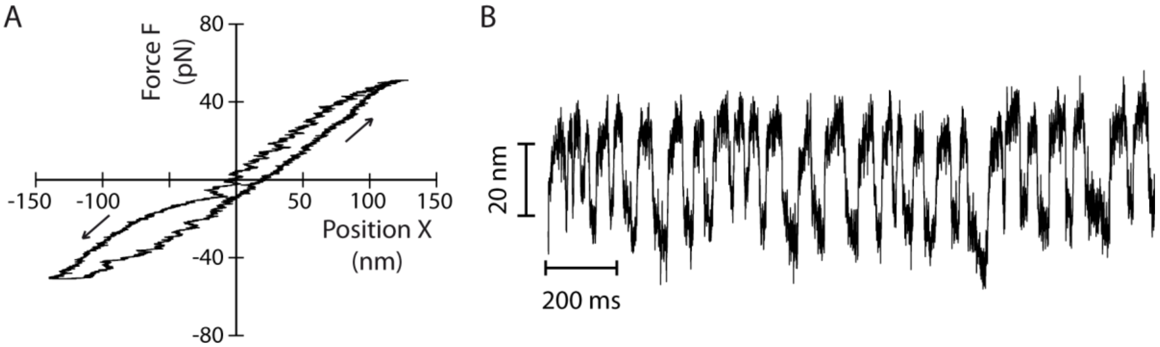

Fig. S3. Hair-bundle activity. ***(A)*** *Counterclockwise force-displacement cycle (arrows) in response to a triangular movement of the stimulus fiber's base at a velocity of 1* $\mu m \cdot s^{-1}$*. Note that oscillations are visible at the beginning of each half cycle, although the relation represents the average of 4 cycles of stimulation.* ***(B)*** *Spontaneous oscillations of the same hair bundle at ~12 Hz. Here, the fiber's base was fixed at position* $\Delta = 0$*. Same cell as in Figs. 1-3 in the main text.*

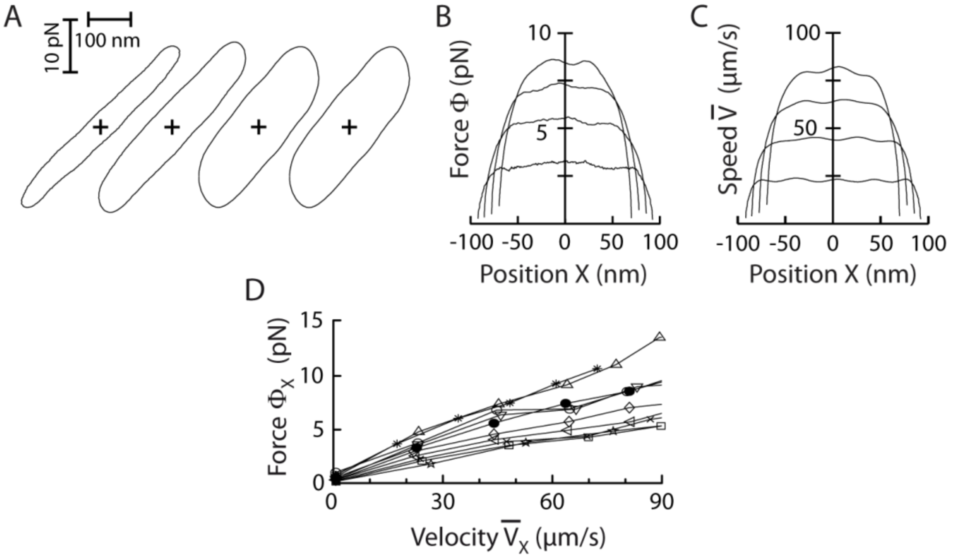

Fig. S4. Hair-bundle mechanics with disrupted tip links. *A hair bundle had its tip links severed by briefly applying the calcium chelator BAPTA.* ***(A)*** *The external force F,* ***(B)*** *the friction estimate* Φ*, and* ***(C)*** *the mean bundle velocity* $\bar{V}$ *are plotted, respectively, as a function of bundle position X for different velocities of triangular motion of the stimulus fiber's base. Crosses in the hysteretic force-displacement cycles shown in A mark the origin* ($X = 0, F = 0$) *of the plots.* ***(D)*** *Force* Φ *at* $X = 0$*, noted* Φ_X*, as a function of bundle velocity* $\bar{V}_X$ *at this position for 10 different cells (black disks corresponds to the data shown in A-C). We performed linear fits to each of these relations; the ensemble average of the fits is shown in Figs. 3C of the main text.*

Section 2: **Mechanical description of a stimulus fiber**

Triangular waveforms of motion applied at the base of a flexible stimulus fiber result in complex, frequency-dependent drag forces along the length of the fiber. These drag forces are important because they affect the magnitude of the external force exerted by the fiber at its tip on an attached hair bundle. In this section, we show analytically how measurements of the fiber's tip and base movements in a viscous fluid allow for a precise computation of the external force exerted by the fiber.

The stimulus fiber is described as a slender rod of length L immersed in a viscous fluid. A time-dependant movement $\Delta(t)$ is applied at the fiber's base in a direction perpendicular to the fiber's axis. As the result of frictional forces distributed along the whole length of the fiber and of the point load $F_{HB}(t)$ exerted by an attached hair bundle at the fiber's tip, the fiber bends. The two-dimensional bending profile is characterized by a function $u(y,t)$ of position y and time t (Fig. Fig. ***S5***).

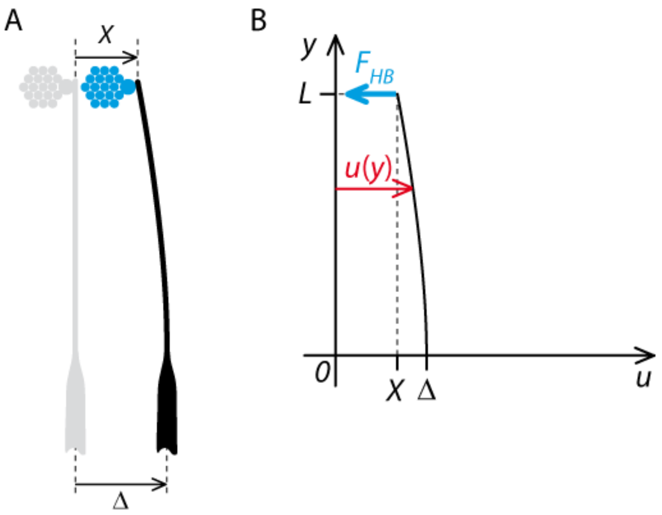

Fig. S5. Geometry of a stimulus fiber. *(A) Schematic representation of a stimulus fiber attached to a hair-cell bundle. A movement Δ imposed at the fiber's base results in a motion X at the fiber's tip. (B) Bending profile u(y) of the fiber. The bundle exerts a point force* F_{HB} *at y = L.*

To describe the mechanical properties of the fiber, we introduce a friction coefficient per unit length ξ, associated to movements perpendicular to the rod's axis, and a flexural rigidity $\kappa = EI$

that characterizes the fiber's elastic resistance to bending forces. Here, E is the Young's modulus and I is the geometrical moment of inertia of the cross-section. Assuming that the fiber is cylindrical and homogeneous, the parameters ξ and κ do not vary along the length of the fiber. The beam equation states that the bending moment M at position y, which results from all the forces exerted at positions $y \leq y' \leq L$, is proportional to the local curvature (1, 2). For small deflections, this condition can be written as:

$$M(y,t) = F_{HB}(t) \times (L-y) + \int_y^L f_v(y',t) \times (y'-y)\, dy' \cong \kappa \frac{\partial^2 u}{\partial y^2}(y,t)\,, \tag{S1}$$

in which $f_v = -\xi \frac{\partial u}{\partial t}$ is the drag force per unit length. Taking the second derivative of Equation S1 with respect to y, we get a differential equation that reflects force balance per unit length of the fiber (3, 4):

$$\xi \frac{\partial u}{\partial t} = -\kappa \frac{\partial^4 u}{\partial y^4}\,. \tag{S2}$$

2.1. Force exerted by a stimulus fiber on a hair-cell bundle

We aim at calculating the force F(t) exerted by the fiber on a hair bundle (or any other object) attached at the fiber's tip. Because of mechanical reciprocity, this force is the opposite of the external force F_{HB}(t) applied on the fiber's tip and given by:

$$F(t) = -F_{HB}(t) = \kappa\, u'''(y=L,t)\,. \tag{S3}$$

Here and in the following, primes denote spatial derivatives. The force can thus be derived from the bending profile of the fiber.

To solve the hydrodynamic beam equation (Eq. S2), we consider a stimulus resulting from a periodic movement $\Delta(t)$ of the fiber's base, as is the case in our experiments. We can then write the stimulus as a Fourier series:

$$\Delta(t) = \mathrm{Re}\left(\sum_{n=0}^{+\infty}\left[\tilde{\Delta}_n\, e^{-in\,\omega_0 t}\right]\right), \tag{S4}$$

where $i^2 = -1$, $T = 2\pi/\omega_0$ is the period of the stimulus, $\widetilde{\Delta}_n = \frac{2}{T}\int_0^T \Delta(t)\ e^{+in\,\omega_0 t}\, dt$ for $n \geq 1$ and $\widetilde{\Delta}_0 = \langle \Delta(t) \rangle$. In turn, the response $X(t) = \mathrm{Re}\left(\sum_{n=0}^{+\infty}\left[\tilde{X}_n\, e^{-in\,\omega_0 t}\right]\right)$ and the profile $u(y,t) =$

Re$\left(\sum_{n=0}^{+\infty}\left[\tilde{u}_n\,(y)\; e^{-in\,\omega_0 t}\right]\right)$ follow similar expressions. Using the variable $\bar{y} = y/L$, Equation S2 indicates that each Fourier component of the profile obeys:

$$\tilde{u}_n''''(\bar{y}) = \alpha_n^4\, \tilde{u}_n(\bar{y})\ . \tag{S5}$$

We have here introduced the adimensional number

$$\alpha_n^4 = \ i\; n\; \omega_0/\omega_S\ , \tag{S6}$$

in which

$$\omega_S = \kappa/(\xi L^4)\ , \tag{S7}$$

is a characteristic elasto-hydrodynamic frequency (5) and $n\omega_0$ is the frequency of the n$^{\text{th}}$ Fourier component ($n \geq 1$). The modulus of the number defined in Equation S6 compares the magnitudes of frictional and elastic forces at angular frequency $n\omega_0$.

Equation S2 contains a fourth-order derivative; we thus need four boundary conditions to determine the profile $u(y,t)$. Because the fiber is clamped at its base ($y = 0$), we must impose $u(y=0,t) = \Delta(t)$ and $u'(0,t) = 0$. In addition, at $y = L$, the position of the fiber is that of the hair bundle and there is no torque: $u(y = L, t) = X(t)$ and $u''(L,t) = 0$. Correspondingly, the solution to Equation S5 must obey $\tilde{u}_n(0) = \tilde{\Delta}_n$, $\tilde{u}_n'(0) = 0$, $\tilde{u}_n(1) = \tilde{X}_n$, and $\tilde{u}_n''(1) = 0$. Using the Ansatz

$$\tilde{u}_n(\bar{y}) = A_n\ \cosh(\alpha_n\bar{y}) + B_n\ \sinh(\alpha_n\bar{y}) + C_n\ \cos(\alpha_n\bar{y}) + D_n\ \sin(\alpha_n\bar{y})\ , \tag{S8}$$

we find the solution to Equation S5 with:

$$A_n = \left[-\tilde{X}_n\ (\sinh\alpha_n + \sin\alpha_n) + 2\,\tilde{\Delta}_n\,(\cos\alpha_n\ \times \sinh\alpha_n)\right]/E_n\ ,$$

$$B_n = \left[\tilde{X}_n\ (\cos\alpha_n + \cosh\alpha_n) - 2\,\tilde{\Delta}_n\,(\cos\alpha_n\ \times \cosh\alpha_n)\right]/E_n,$$

$$C_n = \left[\tilde{X}_n\ (\sinh\alpha_n + \sin\alpha_n) - 2\,\tilde{\Delta}_n\,(\cosh\alpha_n\ \times \sin\alpha_n)\right]/E_n,$$

$$D_n = \left[-\tilde{X}_n\ (\cos\alpha_n + \cosh\alpha_n) + 2\,\tilde{\Delta}_n\,(\cos\alpha_n\ \times \cosh\alpha_n)\right]/E_n,$$

and the denominator $E_n = 2\,(\cos\alpha_n \times \sinh\alpha_n - \sin\alpha_n \times \cosh\alpha_n)$. From Equation S3, we then calculate the Fourier components $\tilde{F}_n = (\kappa/L^3)\ u_n'''(\bar{y} = 1)$ of the force

$$F(t) = \mathrm{Re}\left(\sum_{n=0}^{+\infty}\left[\tilde{F}_n\, e^{-in\,\omega_0 t}\right]\right) \tag{S9}$$

applied by the fiber at its tip:

$$\tilde{F}_n = \frac{\kappa}{L^3}\,\alpha_n^3\left[\frac{1+\cos\alpha_n\times\cosh\alpha_n}{\cos\alpha_n\times\sinh\alpha_n-\sin\alpha_n\times\cosh\alpha_n}\,\tilde{X}_n - \frac{\cos\alpha_n+\cosh\alpha_n}{\cos\alpha_n\times\sinh\alpha_n-\sin\alpha_n\times\cosh\alpha_n}\,\tilde{\Delta}_n\right]. \quad \text{(S10)}$$

From measurements of the fiber's tip $X(t)$ and base $\Delta(t)$ movements, we can compute their Fourier components and in turn use Equations S9-S10 to calculate the external force $F(t)$ applied to the hair bundle. The only unknowns here are the typical fiber stiffness κ/L^3 and drag ξL, whose ratio set the characteristic elasto-hydrodynamic frequency $\omega_S = \kappa/(\xi L^4)$ and in turn the values of the parameters α_n. As we shall see below (paragraph 2.3), stiffness and drag can be estimated by analyzing the thermal fluctuations of the fiber's tip.

2.2. Low-frequency limit of the stimulus force

In the low-frequency limit $|\alpha_1| \ll 1$, we can expand $\tilde{F}_n$ (Eq. S10) in powers of $n\omega_0$. Keeping the first-order term only, we find:

$$\tilde{F}_n \cong k_F\big(\tilde{\Delta}_n - \tilde{X}_n\big) + in\omega_0\,\big(\lambda_{XX}\,\tilde{X}_n + \lambda_{\Delta X}\,\tilde{\Delta}_n\big), \quad \text{(S11)}$$

in which we recognize the stiffness of a cantilever beam (2)

$$k_F = 3\kappa/L^3 \quad \text{(S12)}$$

and the friction coefficients

$$\lambda_{XX} = \frac{33}{140}\xi L \quad \text{(S13)}$$

and

$$\lambda_{\Delta X} = \frac{39}{280}\xi L. \quad \text{(S14)}$$

In the temporal domain (Eq. S9), the force can then be written as:

$$F(t) \cong k_F(\Delta - \mathrm{X}) - \lambda_{XX}\,\dot{X} - \lambda_{\Delta X}\,\dot{\Delta}. \quad \text{(S15)}$$

In the low-frequency limit, a movement of the fiber's base produces a force that can be written as a linear combination of elastic and frictional contributions (6). For positive movements of both the fiber's base and tip, the force applied by the fiber can be much smaller than the elastic force that would be measured if the fiber assumed a static deflection of the same magnitude. Note that

$\lambda_{\Delta X} = (13/22)\,\lambda_{XX} \cong 0.6\,\lambda_{XX}$ is of the same order of magnitude as λ_{XX}. Because in our experiments $\dot{\Delta} \geq \dot{X}$, movements of the fiber's base results in significant friction at the fiber's tip. This contribution to the external force had been ignored in earlier dynamic force measurements (7); omitting it here would result in a large overestimation of viscous drag on the hair bundle.

2.3. Stiffness and drag from thermal fluctuations at the tip of a stimulus fiber

We show here how the typical fiber stiffness κ/L^3 and the characteristic elasto-hydrodynamic frequency ω_S can be extracted from the power spectrum of thermal fluctuations of the free fiber's tip. These parameters are necessary and sufficient to calculate the force exerted by the fiber on the bundle (Eqs. S9-S10).

We consider that the fiber's base is held at a fixed position $\Delta = 0$ and that no external force is applied at its tip ($F_{HB} = 0$). The bending profile $u(y,t)$ must solve the hydrodynamic beam equation (Eq. S2) with the boundary conditions:

$$u(0,t) = 0,\, u'(0,t) = 0\,,\, u''(L,t) = 0\,, \text{ and } u'''(L,t) = 0\,. \tag{S16}$$

The solution can be written as a sum of modes (4):

$$u(y,t) = \textstyle\sum_n a_n(t)\, u_n(y), \tag{S17}$$

with

$$a_n(t) \propto \exp(-\omega_n t), \tag{S18}$$

$$u_n(y) = \cos\left(\beta_n \frac{y}{L}\right) - \cosh\left(\beta_n \frac{y}{L}\right) - A_n \cdot \left(\sin\left(\beta_n \frac{y}{L}\right) - \sinh\left(\beta_n \frac{y}{L}\right)\right). \tag{S19}$$

There, $A_n = \left(\cos(\beta_n) + \cosh(\beta_n)\right)/\left(\sin(\beta_n) + \sinh(\beta_n)\right)$ and the number β_n is solution of $\cos(\beta_n) \times \cosh(\beta_n) = -1$.

We note that the spatial eigen-modes u_n are orthogonal with $\int_0^L u_m(y)\, u_n(y)\, dy = L \cdot \delta_{nm}$, where δ_{nm} is the Kroenecker delta. In addition, the eigen-frequency ω_n of mode n obeys:

$$\omega_n = \omega_S \cdot (\beta_n)^4, \tag{S20}$$

in which ω_S is given by Equation S7.

To describe the thermal fluctuations of the fiber's profile, we add a noise term η to the hydrodynamic beam equation (Eq. S2):

$$\xi \frac{\partial u}{\partial t} = -\kappa \frac{\partial^4 u}{\partial y^4} + \eta(t, y)\ . \tag{S21}$$

We use Gaussian white noise. The noise term is zero on average and its intensity is characterized by the autocorrelation:

$$\langle \eta(t, y)\, \eta(t', y') \rangle = 2k_B T\, \xi\, \delta(t - t')\, \delta(y - y')\ . \tag{S22}$$

Combining Equation S21 with Equations S17-S19, we get:

$$\frac{da_n}{dt} = -\omega_n a_n + \eta_n/(\xi L)\ , \tag{S23}$$

in which $\eta_n(t) = \int_0^L \eta(y, t)\, u_n(y)\, dy$ and $\langle \eta_n(t)\, \eta_m(t') \rangle = 2k_B T\, (\xi L)\, \delta_{nm}\, \delta(t - t')$. Using tildes to denote Fourier transforms, with for instance $\tilde{a}_n(\omega) = \int_{-\infty}^{+\infty} a_n(t)\, e^{+i\omega t}\, dt$, Equation S23 yields:

$$\tilde{a}_n(\omega) = \frac{1}{\omega_n - i\omega} \times \frac{\tilde{\eta}_n(\omega)}{\xi L}, \tag{S24}$$

with $\langle \tilde{\eta}_n(\omega)\, \tilde{\eta}_m(\omega') \rangle = 4\pi k_B T\, (\xi L)\, \delta_{nm}\, \delta(\omega - \omega')$. The power spectrum $\tilde{C}(\omega)$ of the fiber's tip is defined by:

$$\langle \tilde{u}(L, \omega) \tilde{u}^*(L, \omega') \rangle = 2\pi\ \delta(\omega - \omega')\, \tilde{C}(\omega)\ . \tag{S25}$$

Combining Equations S17, S24, and S25, we get:

$$\tilde{C}(\omega) = \frac{2\, k_B T}{\lambda} \sum\nolimits_n \frac{1}{\omega_n^2 + \omega^2}\ , \tag{S26}$$

in which we have used $u_n^2(L) = 4$ and introduced the friction coefficient $\lambda = \xi L/4$.

Being a sum of Lorentzians, the power spectrum is not a Lorentzian. However, because $\omega_2/\omega_1 = (\beta_2/\beta_1)^4 = 39.27$, the first mode dominates at low frequencies. We can thus approximate $\tilde{C}(\omega)$ by a single Lorentzian (8, 9):

$$\tilde{C}(\omega) \cong \frac{2\, k_B T}{\lambda} \frac{1}{\omega_1^2 + \omega^2}\ . \tag{S27}$$

The fiber is then characterized by the stiffness $k = \omega_1 \lambda$ associated to the first mode of vibrations.

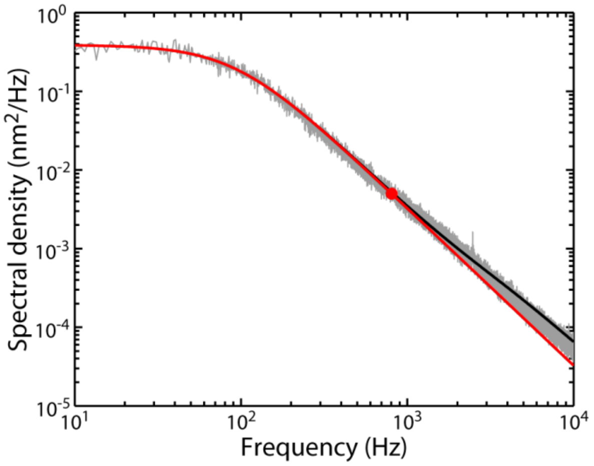

Fig. S6. Fluctuations of a stimulus fiber. *This doubly-logarithmic plot shows the power spectral density of motion of a stimulus fiber's tip as a function of frequency (grey). A Lorentzian fit to the power spectrum (red line) yields the stiffness* $k = 71\ \mu N\cdot m^{-1}$, *the drag coefficient* $\lambda = 124\ nN\cdot s\cdot m^{-1}$, *and the cutoff frequency* $f_c = 92\ Hz$. *The fit was restricted to frequencies below the abscissa of the red disk but is here plotted over the whole frequency range. Identifying the cutoff frequency with the characteristic frequency* $\omega_1/(2\pi)$ *of the first mode of fiber fluctuations allowed for the calculation of the frequencies* $\omega_n = \omega_1(\beta_n/\beta_1)^4$ *of all the other modes and thus for an estimate of the full spectrum (Eq. S26; black line). The first mode dominates the spectrum at frequencies below 1 kHz, corresponding to frequencies* $f \leq 10 \times f_c$, *but deviations become apparent at higher frequencies. The thermal fluctuations of a fiber's tip were recorded for 30 s at a sampling rate of 25 kHz. To get a high dynamical range, we chose here a fiber that was significantly softer than those actually used in our force measurements.*

A fit to the data with Equation S27 provides an estimate of the elasto-hydrodynamic frequency:

$$\omega_S = \omega_1/\beta_1^4 \tag{S28}$$

This parameter is required to compute the force $F(t)$ (Eqs. S6, S9-S10) exerted by a periodic stimulus on a hair bundle attached at the fiber's tip as well as its low-frequency approximation (Eq. S15). For the latter, we have:

$$k_F = (12/\beta_1^4) \cdot k \cong 0.97\ k\ , \tag{S29}$$

$$\lambda_{XX} = \frac{33}{35}\lambda \cong 0.94\ \lambda\ , \tag{S30}$$

$$\lambda_{\Delta X} = \frac{39}{70}\lambda \cong 0.57\ \lambda\ . \tag{S31}$$

With typical values $k = 200\ \mu N\cdot m^{-1}$ and $\lambda = 100\ nN\cdot s\cdot m^{-1}$, we get $\omega_1 = 2000\ rad\cdot s^{-1}$. This yields an elasto-hydrodynamic frequency $\omega_S = 162\ rad\cdot s^{-1}$. For a triangular waveform of motion $\Delta(t)$ with a peak-to-peak amplitude of 600 nm, the condition $|\alpha_1| \ll 1$ for applying the low-frequency approximation of the force (Eq. S15) calls for velocities of the fiber's base $|\dot{\Delta}| \ll 30\ \mu m\cdot s^{-1}$.

Because we applied fiber's velocities up to 300 µm·s^{-1}, we expect the low-frequency estimate to deviate significantly from the exact expression given by Equations S9-S10. We quantify the deviation below.

2.4. Experimental test of force measurements with a stimulus fiber

To test both the validity and the accuracy of our force measurements, we analyzed the behavior of a stimulus fiber under circumstances for which the fiber's tip is not attached to any accessory structure and is thus free to move in the fluid. As in regular experiments, we measured the position of the fiber's tip $X(t)$ in response to symmetric triangular waveforms of motion $\Delta(t)$ of the base (see *Materials and Methods* in main text). As a result of viscous drag exerted by the surrounding fluid, the fiber is expected to bend ($X \neq \Delta$). Because the tip is here unconstrained, however, the fiber's elastic resistance to bending and the drag force must be equal and opposite: the estimated net force F at the fiber's tip should be null ($F = -F_{HB} = 0$ in Fig. Fig. S5B).

When we used the exact harmonic solution to the hydrodynamic beam equation (Eq. S2), we calculated forces (Eqs. S9-S10) that were indeed very low in magnitude (Fig. S7A). Although the force could grow proportionally to the tip position, especially at large velocities (red line in Fig. S7A), the resulting absolute slope was less than 25 µN·m^{-1}, which is only 2.5% the stiffness of an intact hair bundle. An error in the calibration of the photometric system that was used to measure tip positions could easily explain the parasitic stiffnesses that were measured. In addition, the force-displacement relation displayed very little hysteresis over a cycle of stimulation (Fig. S7A). Correspondingly (Fig. S7B), the friction estimate Φ, defined as half the vertical height of the hysteretic cycle (see section 3), was less than half a piconewton at all positions (±300 nm) and over the whole velocity range (1-300 µm·s^{-1}) that we explored.

At low velocities (<35 µm·s^{-1}), the low-frequency approximation of the force (Eq. S15) provided a satisfactory representation of the full estimate (blue line in Fig. S7A and C), as expected. However, as the fiber velocity increased, hysteresis appeared near the extremes of fiber motion, where the fiber abruptly reversed its direction of motion and thus excited high-frequency modes of fiber deformation. Correspondingly, the friction estimate Φ peaked in this range of positions. Near the center of the periodic movement ($X = 0$), the friction estimate remained near zero for velocities up 150 µm·s^{-1} (Fig. S7E). However, as they grew in magnitude and broadened with stimulation velocity, the friction peaks eventually merged, resulting in apparent friction forces even in the center.

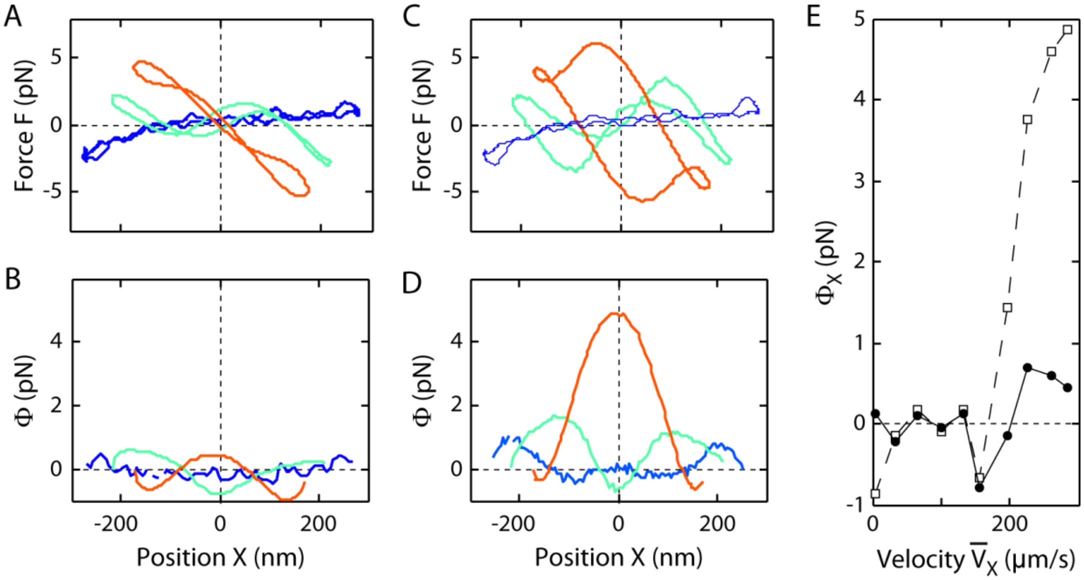

Fig. S7. ***Force estimated at the tip of a free fiber moving in water.*** *Symmetric triangular waveforms of motion $\Delta(t)$ were applied to the fiber's base at three different velocities (blue: 34 µm·s^{-1}, green: 155 µm·s^{-1}, red: 285 µm·s^{-1}).* ***(A)*** *and* ***(C):*** *Force F exerted by the fiber's tip as a function of tip position X.* ***(B)*** *and* ***(D):*** *Force Φ, calculated as half the vertical height of the hysteretic cycles shown in* ***A*** *and* ***C****, as a function of tip position.* ***(E)*** *Force Φ at X = 0, noted Φ_X, as a function of tip velocity, $\overline{V}_X$, at this position. The forces were estimated by using either Equations S9-S10 (panels* ***A****,* ***B*** *and black disks in panel* ***E****) or the low-frequency approximation given by Equation S15 (panels* ***C****,* ***D*** *and white squares in panel* ***E****). The mechanical properties of the fiber were calibrated by extracting the effective stiffness $k = 162 \pm 3$ µN·m^{-1} (mean ± SD; n = 2) and friction coefficient $\lambda = 123 \pm 4$ nN·s·m^{-1} (mean ± SD; n = 2) from the thermal fluctuations of the fiber's tip (Eq. S27).*

Section 3: **Friction estimate from hysteresis in the relation between external force and position**

In this section, we discuss how to estimate friction forces by analyzing hysteresis in the relation between external force and position. We first consider the simple case of a passive system that undergoes a cyclic movement. A positive movement from position X_{min} to position X_{max} is followed by the reverse movement from X_{max} to X_{min}. During the positive half cycle, the system at position X is subjected to an external force $F^{+}(X)$. For a small positive displacement dX from position X, the work $dW^{+} = F^{+}\, dX$ is performed on the system. A part dU^{+} of this work changes the potential energy U, while the remaining part $dW_d^{+} = dW^{+} - dU^{+}$ is dissipated in the thermal bath. The force $F_d^{+} = dW_d^{+}/dX$ is the friction force associated with energy dissipation. We can also define an elastic force, also called reactive, $F_r^{+} = dU^{+}/dX$. The total force F^{+} is then the sum of the reactive and dissipative forces: $F^{+} = F_r^{+} + F_d^{+}$. Similarly, if we consider the reverse process, which corresponds to the negative half cycle, the applied force is $F^{-}(X)$. For a displacement –dX from position X, the performed work is $dW^{-} = -F^{-}\, dX$. The applied force can be written as $F^{-} = F_r^{-} - F_d^{-}$, in which F_r^{-} and F_d^{-} are the reactive and dissipative forces, respectively. Note that the reactive force does not change sign when the directionality of motion is reversed $(dX \rightarrow -dX)$, whereas the dissipative force does.

The dissipated work during a cycle is

$$W_d^{+} + W_d^{-} = \int_{X_{min}}^{X_{max}} [F^{+}(X) - F^{-}(X)]\, dX \ . \tag{S32}$$

Because reactive terms do not contribute to dissipation, the reactive forces obey:

$$\int_{X_{min}}^{X_{max}} [F_r^{+}(X) - F_r^{-}(X)]\, dX = 0 \ . \tag{S33}$$

To ensure this condition for any choice of X_{min} and X_{max}, we must impose

$$F_r^{+}(X) = F_r^{-}(X) \ . \tag{S34}$$

Based on these properties, we introduce the force

$$\Phi(X) = [F^{+}(X) - F^{-}(X)]/2 \ , \tag{S35}$$

which, using Equation S34, can also be written as

$$\Phi(X) = [F_d^+(X) + F_d^-(X)]/2 \ . \tag{S36}$$

This expression shows that $\Phi(X)$ is purely dissipative and can thus be interpreted as a friction force.

We now consider a system that displays inversion symmetry with respect to a specific reference point at position X_0 (see Fig. S1). Without loss of generality, we set $X_0 = 0$. Inversion symmetry imposes that we can write:

$$F^+(X) - F_0 = -(F^-(-X) - F_0) \ , \tag{S37}$$

where $F_0 = [F^+(0) + F^-(0)]/2$. From Equation S37, we find that $F_d^-(X) = F_d^+(-X)$ and thus

$$\Phi(X) = [F_d^+(X) + F_d^+(-X)]/2 \tag{S38}$$

This shows that $\Phi(X) = \Phi(-X)$ is symmetric and that $\Phi(X)$ is the average of two dissipative forces on the positive half cycle. In addition at $X = 0$, $F_d(0) = F_d^+(0)$ is the true dissipative force.

One can generalize this formalism to active systems subjected to external forces. In this case, energy resources of biochemical origin can be transduced into mechanical work. The change of potential energy is $dU^\pm = dW^\pm - dW_d^\pm + dW_a^\pm$, where $dW_a^\pm$ is the chemical work performed during a positive or negative half-cycle, respectively. We introduce the active force $F_a^\pm = dW_a^\pm/dX$, such that

$$F^\pm = F_r^\pm \pm F_d^\pm - F_a^\pm \ . \tag{S39}$$

Over one cycle, the total dissipated energy is now given by:

$$W_d^+ + W_d^- = W_a^+ + W_a^- + \int_{X_{min}}^{X_{max}} [F^+(X) - F^-(X)]\, dX \ . \tag{S40}$$

As a result, hysteresis in the relation between the external force and position cannot be attributed solely to the effect of dissipative forces. Active forces contribute additive work, which can be of positive or negative sign. In the latter case, as in our experiments (Fig. S3), activity can result in counterclockwise circulation around the hysteretic cycle and thus the net work performed by the external force over a cycle can be negative. The total energy dissipated (left-hand side of Eq. S40), however, is always positive. From Equations S39 and S40, we obtain that Equations S33 and S34 hold again. The force Φ defined by Equation S35 can then be written as:

$$\Phi(X) = [F_d^+(X) + F_d^-(X) - F_a^+(X) + F_a^-(X)]/2 \tag{S41}$$

The active force contributes to the force Φ. Thus, hysteresis in the force-displacement relation can yield a good estimate of the mean dissipative force only under conditions for which the effects of the active process can be neglected.

Section 4: **Theory of friction from transduction channels' gating forces**

This section describes analytically how friction forces emerge from the gating-spring model of mechanoelectrical transduction when the finite activation kinetics of the transduction channels is taken into account. We ignore here viscous drag and adaptation. We consider that the hair bundle follows a symmetric triangular waveform of motion $X(t)$ as a function of time, with $X_{MIN} \leq X \leq X_{MAX}$ and $X_{MIN} = -X_{MAX}$. On each ramp, the velocity is thus constant with $V^{+}(X) = -V^{-}(X) = V$. Here and in the following, the superscripts denote the directionality of bundle motion. By convention, a positive movement increases tip-link tension and, in turn, the open probability of the transduction channels.

4.1. Delayed gating of the transduction channels

The transduction apparatus of the hair bundle is composed of N transduction channels that operate in parallel (10) and that are each mechanically connected to an elastic gating spring. A transduction channel is described by two states, open or closed (Fig. S8A), and assumes an open probability P_o. In the gating-spring model of mechanoelectrical transduction (11, 12), the energy difference $\Delta G(X) = -Z \times (X - X_0)$ between the two states is a linear function of bundle position X. In this relation, the parameter Z represents the reduction in gating-spring tension —the gating force— upon channel opening and X_0 is the position at which the two states have the same energy. At thermal equilibrium, the channels' open probability $P_o = P_\infty$ is related to bundle position by the Boltzmann function

$$P_\infty = 1/[1 + \exp(-(X - X_0)/\delta)]. \tag{S42}$$

The open probability varies from 5% to 95% over a narrow range of deflections 6δ, where $\delta = (k_B T)/Z$ is a lengthscale that characterizes the mechanosensitivity of the transduction apparatus and $k_B T$ is the thermal energy. Without loss of generality, we set $X_0 = 0$ and thus $P_\infty(X_0) = 1/2$.

When the bundle moves, the open probability changes. However, because channel equilibration is not instantaneous (11, 13), the open probability does not equal its equilibrium value ($P_o \neq P_\infty$). Using first-order kinetics, channel activation can be described by a relaxation process:

$$\tau_c \frac{dP_o}{dt} = P_\infty - P_o \ , \tag{S43}$$

in which the activation time $\tau_c = 1/(k_{co} + k_{oc})$ is the inverse sum of the transition rate k_{co} between the closed and open states of the channel and the rate k_{oc} for the reverse transition (Fig. S8A). Combining the gating-spring model of mechanoelectrical transduction with Kramers' theory for thermally-activated barrier crossing (11), we write that the transition rates depend on the position of the hair bundle as:

$$k_{co}(X) = k_o \exp(\alpha \ X/\delta) \ , \tag{S44}$$

$$k_{oc}(X) = k_o \exp(-(1-\alpha) \ X/\delta) \ . \tag{S45}$$

In these equations, $k_o = k_{co}(0) = k_{oc}(0)$ is the transition rate for $X = 0$, which corresponds here to $P_\infty = 1/2$, and the dimensionless parameter $0 \leq \alpha \leq 1$ represents the fractional distance to the transition state. The activation time is then given by:

$$\tau_c(X) = 2 \ \tau \ /[\exp(\alpha \ X/\delta) + \exp(-(1-\alpha) \ X/\delta)] \ , \tag{S46}$$

where $\tau = 1/(2k_0)$ is the activation time for small deflections near an open probability of 1/2. The relation $\tau_c(X)$ between the activation time and position is bell-shaped with a maximum at X= 0 (Fig. S8B). In the following, we consider the case $\alpha = 1/2$, for which the transition state is positioned half-way in between the open and closed states of the channels (see a discussion of this choice in the paragraph 4.4). Under such condition, the relation $\tau_c(X) = \ \tau \ /\cosh(X/(2\delta))$ is an even function of position X.

For a ramp of positive motion, we write $X = X_{MIN} + Vt$. In the limit of large displacements ($X_{MIN} \rightarrow -\infty$), the integration of Equation S43 yields:

$$P_o^+(X) = \frac{1}{V\tau} \int_{-\infty}^{X} P_\infty(u) \times \mathrm{M}(X,u) \ du, \tag{S47}$$

in which we have introduced the memory kernel

$$\mathrm{M}(X,u) = \cosh(u/(2\delta)) \times \exp\left[-2\frac{\delta}{V\tau}\left[\sinh(X/(2\delta)) - \sinh(u/(2\delta))\right]\right]. \tag{S48}$$

On the way back, the position varies as $X = -X_{MIN} - Vt$. We find that the open probability obeys the symmetry relation:

$$P_o^-(X) = 1 - P_o^+(-X). \tag{S49}$$

If the channels were able to equilibrate instantaneously ($\tau = 0$), their open probability would be given by the steady-state value (Eq. S42) and thus would not depend on the directionality of bundle motion: $P_o^+(X) = P_o^-(X) = P_\infty(X)$. Because channel activation takes time (Eq. S43), however, the channels' open probability depends on the history of bundle motion, i.e. on past positions (Eq. S47). As a result,

$$P_o^+(X) < P_\infty(X) < P_o^-(X). \tag{S50}$$

The relation between open probability and position displays hysteresis and it takes larger displacements, in the positive and negative directions, to open and close half the channels, respectively, than for quasi-static deflections (Fig. S8C-D). In the following, we refer to the width of the hysteretic cycle $P_o(X)$ at $P_o = 0.5$ as the "gating shift". At low velocities ($V \ll V_c = \delta/\tau$), the memory kernel $\mathrm{M}(X,u) \cong \exp(-(X-u)/(V\tau))$. For small deflections ($0 < X \ll \delta$), we can use the linear expansion $P_\infty(u) \cong 0.5 + u/(4\delta)$. Using Equation S47, we then find $P_o^+(X) \cong 1/2 + (X - V\tau)/(4\delta)$. Thus, when the bundle moves in the positive direction, the deflection $X_{0.5}^+$ at which half the channels are open is given by:

$$X_{0.5}^+ \cong V\tau \tag{S51}$$

Because $X_{0.5}^- = -X_{0.5}^+$ (Eq. S49), the gating shift $\Delta X = X_{0.5}^+ - X_{0.5}^- = 2 \times V\tau$ increases in proportion to velocity with a slope that provides twice the characteristic activation time τ (Fig. S8D). Note that $P_o^\pm(X) \cong P_\infty(X) \mp V\tau/(4\delta)$. At high velocities ($V \gg V_c$), $P_o^+(X) \cong \mathcal{H}(X) \times \{1 - \exp[-2\delta/(V\tau) \times \sinh(X/(2\delta))]\}$, where $\mathcal{H}$ is the Heaviside step function. We then get:

$$X_{0.5}^{+} \cong 4\delta\ \mathrm{Log}(V). \tag{S52}$$

Thus, the gating shift displays a sublinear growth with velocity (Fig. S8D).

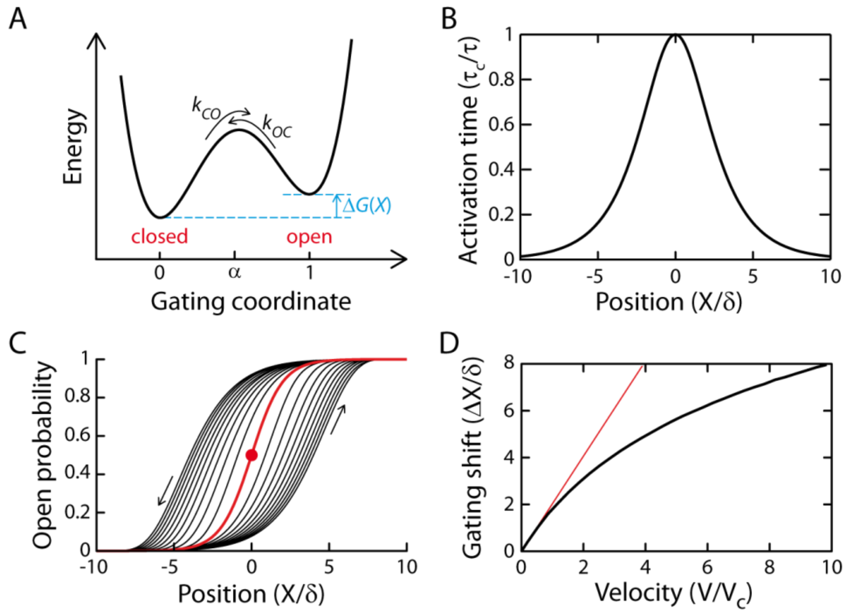

Fig. S8. Hysteresis from finite activation kinetics of the transduction channels. ***(A)*** *Schematic energy landscape of a transduction channel with two states (open and closed). The transition state resides at a fractional distance α from the closed state. The channel switches between its two states with rate constants k_{CO} and k_{OC}. The energy difference $\Delta G(X)$ between the two states depends on bundle position X.* ***(B)*** *The activation time of the channel is plotted as a function of bundle position in the case α = 0.5. Time and position are normalized, respectively, by the activation time τ near $P_\infty = 0.5$, here corresponding to X = 0, and by the characteristic lengthscale δ of mechanosensitivity.* ***(C)*** *Open probability of the transduction channels as a function of the normalized hair-bundle position when the bundle is subjected to a series of symmetric triangular waveforms of motion. Bundle velocity varies from V_c to 10×V_c in 9 steps, where $V_c = \delta/\tau$ is a characteristic velocity. The red curve corresponds to the steady-state relation $P_\infty(X)$. The hysteretic cycles (black) display inversion symmetry with respect to the point marked by a red disk and get broader at increasing bundle velocities. As a result, the larger the velocity, the further the bundle has to move in each direction before the channels can gate. The bundle displays a clockwise circulation around the cycles (arrows).* ***(D)*** *Normalized gating shift as a function of normalized bundle velocity. The tangent going through the origin (red line) has a slope of 2.*

4.2. Hair-bundle friction from delayed gating forces

The direct mechanical coupling between the transduction channels and the gating springs imposes a reciprocal relation between the channels' open probability and gating-spring tension (8, 14). Ignoring viscous drag and adaptation, the relation between the external force F and the hair-bundle position X can be written as:

$$F(X) = K_\infty X - NZ \times (P_o(X) - 0.5) + F_0, \tag{S53}$$

where $F(0) = F_0$ at steady state. For large deflections, the hair bundle behaves as a Hookean spring of stiffness K_∞ that corresponds to the combined stiffness of gating springs and stereociliary pivots. In contrast, within the narrow region of deflections that elicit a significant change of the channels' open probability P_o, gating forces of magnitude Z reduce the slope $dF/dX = K_\infty - NZ\, dP_o/dX$ of the force-displacement relation and thus effectively soften the hair bundle. Gating compliance is maximal where the derivative dP_o/dX is the highest, which happens near $P_o = 0.5$ (Fig. S8C).

When the hair bundle is subjected to triangle stimulation, the channels' open probability at any given position is smaller on the positive half cycle than that on the negative half cycle (Eq. S50, Fig. S8C). As a result, $F^+(X) > F^-(X)$ and the force-displacement relation displays hysteresis (Fig. S9A). Hysteresis reflects the gating shift between the positions $X_{0.5}^{\pm}$ where half the channels are open (Fig. S8C) or, equivalently, between the positions of maximal gating compliance (Fig. S9B). Thus, although there is no explicit source of dissipation, the hair bundle experiences friction. Following the general theory developed in Section 3, the external force $F^\pm = F_r \pm F_d^\pm$ may be written as a combination of a reactive force F_r and of a dissipative force F_d. Note that the reactive force does not depend on the directionality of bundle motion $F_r(X) = F_r^+(X) = F_r^-(X)$ (Eq. S34). At any given position, the reactive force can here be obtained by allowing the transduction channels to reach steady state at this position, i.e. by imposing $P_o = P_\infty$ in the force-displacement relation (Eq. S53):

$$F_r(X) = K_\infty X - NZ \times (P_\infty(X) - 0.5) + F_0. \qquad \text{(S54)}$$

The dissipative component of the external force —the friction force— is then given by:

$$F_d^\pm(X) = \pm NZ\left(P_\infty(X) - P_o^\pm(X)\right). \qquad \text{(S55)}$$

Equation S55 clarifies that friction is here the direct consequence of the finite activation kinetics of the transduction channels, for this property imposes that the open probability $P_o^\pm$ be different than its steady-state value P_∞ (Eq. S43). On each half cycle of triangular motion, the dissipative force depends on position and peaks at the position $X_{max}^\pm\left(\leq X_{0.5}^\pm\right)$ where the slope of the force-displacement relation matches hair-bundle stiffness at steady state (Fig. S9B-C). Note that friction peaks at opposite positions on the positive and negative half cycles.

To estimate the true friction force $F_d^{\pm} = \pm(F^{\pm} - F_r)$, it is necessary to measure both the external force and its reactive component as a function of bundle position. In the case of oscillatory hair bundles, the relation $F_r(X)$ contains an unstable region of negative stiffness that is difficult to measure accurately (14). As demonstrated in Section 3, we can nevertheless characterize friction by measuring the half-height of the hysteretic force-displacement relation:

$$\Phi(X) = [F^{+}(X) - F^{-}(X)]/2. \qquad \text{(S56)}$$

Because $F_r^{+}(X) = F_r^{-}(X)$, the force $\Phi(X) = [F_d^{+}(X) + F_d^{-}(X)]/2$ represents the arithmetic mean of the absolute friction force on the positive half cycle and that on the negative half cycle, at the same position X. Using equation S53, the force Φ can be written as

$$\Phi(X) = (NZ/2)[P_o^{-}(X) - P_o^{+}(X)]. \qquad \text{(S57)}$$

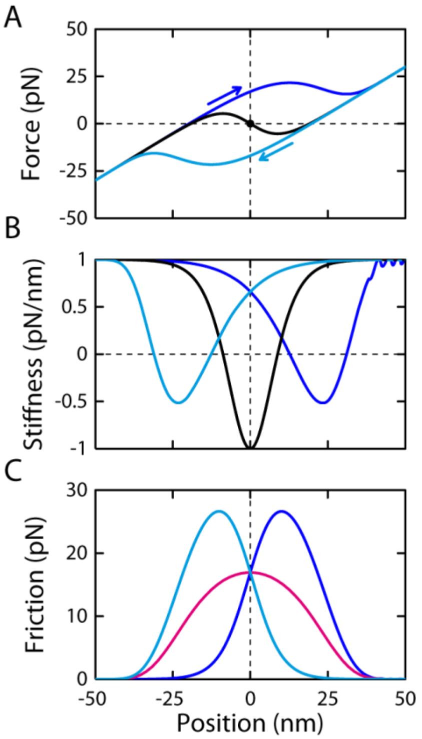

Fig. S9. Channel friction. ***(A)*** *External force F as a function of hair-bundle position X. At steady-state (black line), the external force is purely reactive:* $F(X) = F_r(X)$. *When the hair-bundle follows a triangular waveform of motion, a dissipative force —channel friction— adds to the reactive component of the external force, resulting in a hysteretic cycle. The positive and negative half cycles* $F^{\pm}(X)$ *are shown in blue and cyan (directionality indicated by arrows), respectively. They display inversion symmetry with respect to the origin (black disk).* ***(B)*** *Hair-bundle stiffness, defined as the derivative of the relations shown in* ***A****, is plotted as a function of bundle position. Stiffness (blue and cyan) is minimal at positions* $X_{0.5}^{\pm}$ *nearly, but not precisely, half the channels are open.* ***(C)*** *Dissipative component of the external force* $F_d^{\pm} = \pm(F^{\pm} - F_r)$ *as a function of bundle position (blue and cyan). The relation between the mean friction force* $\Phi(X) = [F_d^{+}(X) + F_d^{-}(X)]/2$ *and bundle position is plotted in magenta. Velocity and amplitude of triangular motion:* $V = 100\ \mu m{\cdot}s^{-1}$ *and A = 100 nm. Parameters in Table S1 (SI Appendix section 5).*

Combining Equation S57 with Equations S47-S49 yields a bell-shaped relation between the mean friction force Φ and bundle position X, with a maximum at the position where half the transduction channels are open at steady state, here $X = 0$ (magenta line in Fig. S9C).

Increasing bundle velocity results in the broadening of the force-displacement cycles (Fig. 4A in main text). At the peak ($X = 0$), the force Φ increases with bundle velocity as:

$$\Phi(X = 0,\ V) = -(NZ/2)\left[\frac{2}{V\tau}\int_{-\infty}^{0} P_{\infty}(u)\ \times \mathrm{M}(X = 0, V, u)\ du - 1\right]. \tag{S58}$$

The relation between channel friction and velocity is nonlinear. When the velocity is large enough that $V\tau$ becomes comparable to the characteristic lengthscale δ, the channel friction force displays a sublinear growth (Fig. S10) that eventually saturates at the maximum value $\Phi_{max} = NZ/2$ at large velocities ($V \gg V_c$).

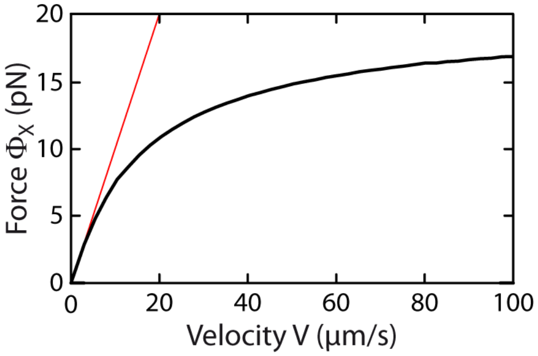

Fig. S10. Effect of bundle velocity on channel friction. *Force Φ at X = 0, noted Φ_X, as a function of bundle velocity V when dissipation comes from transduction channels only. At large velocities, the friction force saturates at $\Phi_{max} = 20\,pN$. The red line represents the initial slope, noted λ_C, of the relation Φ_X(V). Parameters in Table S1 (SI Appendix section 5).*

At low velocities ($V \ll V_c = \delta/\tau$), only the values of u near zero contribute to the integral in Equation S58. In turn, we use the approximations $\mathrm{M}(X = 0, V, u) \cong \exp(u/(V\tau))$ and $P_{\infty} \cong 0.5 + u/(4\delta)$. We then find the linear regime of friction:

$$\Phi(X = 0, V) \cong \lambda_C V, \tag{S59}$$

with the friction coefficient

$$\lambda_C = NZ^2\tau/(4k_BT). \tag{S60}$$

With parameters listed in Table S1, we get $\lambda_C = 1$ µN·s·m^{-1}. This value is orders of magnitude larger than that expected simply from viscous drag associated with conformational changes of the channels moving in a fluid. Indeed, in this case we would estimate a friction coefficient on the order of $\xi_H = N\gamma^2 \times 3\pi\eta d \cong 0.1$ nN·s·m^{-1}. Here, $d = \gamma D$ (see Table S1) corresponds to the size of the conformational change associated to channel gating, $\gamma \cong 0.14$ is the projection factor between tension in the oblique tip link and force along the horizontal axis of bundle stimulation, and we chose a viscosity η comparable to that of water.

4.3. *Channel friction versus viscous drag for low-frequency and auditory hair cells*

Channel friction is expected to provide a significant contribution to hair-bundle mechanics only if the bundle operates in the low-velocity regime of the nonlinear relation $\Phi_X(V)$ (Fig. S10). Indeed, channel friction displays a sublinear growth with velocity, whereas viscous drag on the hair-bundle structure increases in proportion to velocity (15). Viscous drag will thus eventually outgrow channel friction whenever bundle velocities become high enough that the effect of channel gating saturates. This is the case when the bundle velocity V is much larger than the characteristic velocity $V_C = \delta/\tau$, where $\delta = k_B T/Z$ is a lengthscale that we had introduced earlier in Eq. S42, Z is the gating force and τ is the channel activation time. For saccular hair bundles from the bullfrog, we calculate $V_C = 10$ µm/s (parameters in Table S1). The sensitivity of oscillatory hair bundles to periodic stimuli peaks at a characteristic frequency that is near the frequency of spontaneous oscillations (16). A sinusoidal stimulus that evokes a bundle movement at the characteristic frequency (~10 Hz; see Fig. S3) with an amplitude of 10 nm $(= 2\delta)$ moves the bundle at velocity $V \cong 0.6$ µm/s $<< V_C$. In this low-velocity regime, both channel friction and viscous drag increase in proportion to bundle velocity. Consequently, channel friction can be described by the friction coefficient given by Eq. S60; its value is about tenfold larger than that characterizing viscous drag ($\lambda_H \cong 0.1$ µN·s/m; see main text). For stimulation at the cell's characteristic frequency, channel friction thus dominates viscous drag by nearly tenfold. If we now stimulate the same bundle at 1 kHz, the bundle velocity is a thousand times larger and thus $V/V_C >> 1$. Channel friction in turn saturates at its maximal value of 20 pN

(Fig. S10). On the other hand, viscous drag produces a frictional force of 60 pN. At 1 kHz, channel friction is only 25% of the total frictional force; this value drops to 2.5% at 10 kHz.

Does this imply that channel friction has only a marginal effect at auditory frequencies? Auditory frequencies are detected by dedicated hair cells that are endowed with hair bundles that have different characteristics than those of the bullfrog's sacculus. The bundle morphology, in particular the number of stereocilia and their height (17), as well as the channel time (according to (13)), varies systematically with the cell's characteristic frequency. Stereocilia are generally shorter and more numerous, and the transduction channels are faster for auditory hair cells than in the bullfrog's sacculus. Although decreasing the channel time tends to diminish the magnitude of channel friction (Eq. S60), increasing the number of channels and decreasing the bundle height (see below) does the opposite. Therefore, whether or not channel friction is relevant at auditory frequencies depends on the numerical values of these parameters.

As an illustrative example, consider an outer hair cell from the apical turn of the rat cochlea. We again assume a sinusoidal stimulus near the cell's characteristic frequency, which is here ~4 kHz (18). The hair bundle is now composed of $N = 100$ stereocilia and has a height $h = 4$µm. This values are, respectively, about twice and half those of a hair bundle from the frog (19). In these cells, the time course of channel activation (<50 µs) is too fast to be accurately measured by current techniques (13, 20). As a conservative estimate, we use a channel time $\tau = 10$ µs. Because the channel time is 25-fold smaller than the period of the stimulus, the bundle again operates in the low-velocity regime of the relation $\Phi_X(V)$, where channel friction matters (Fig. S10): with an amplitude of motion of 2δ, $V/V_C = 0.5 < 1$. Channel friction is thus nearly proportional to bundle velocity and characterized by the friction coefficient λ_C given by Eq. S60. To compare rat and frog bundles at their respective characteristic frequencies, we assume that the gating-spring stiffness k_{GS} and the gating swing d stay the same in the two types of hair cells. The gating force $Z = \gamma k_{GS} d$ depends on bundle geometry via the projection factor $\gamma \propto 1/h$ (12) that relates forces produced along the oblique axis of the tip links to those measured experimentally. We thus get $\lambda_C^{rat}/\lambda_C^{frog} \cong (N^{rat}/N^{frog}) \times (h^{frog}/h^{rat})^2 \times (\tau^{rat}/\tau^{frog})$, which yields $\lambda_C^{rat} \cong \lambda_C^{frog}/6.25$. On the other hand, the drag coefficient of the rat bundle might be slightly smaller than that in frog, due to the twofold reduction in bundle height (18). Assuming $\lambda_H^{rat} \cong \lambda_H^{frog}/2$ and using $\lambda_C^{frog}/\lambda_H^{frog}$ = 10 (Table S1), we thus find $\lambda_C^{rat}/\lambda_H^{rat} \cong \left(\lambda_C^{frog}/\lambda_H^{frog}\right) \times 1/3 = 3.3$. These arguments suggest that channel friction can be larger than viscous drag even in the case of an auditory hair cell.

4.4. Point-inversion symmetry

Because $P_o^-(X) = 1 - P_o^+(-X)$ (Eq. S49), the force-displacement cycle displays inversion symmetry with respect to the point of coordinates $(X = 0, F = F_0)$: $F^+(X) - F_0 = -(F^-(-X) - F_0)$. As a result, the mean friction force $\Phi(X)$ is an even function of X: $\Phi(X) = \Phi(-X)$. As already discussed in section 3, at the position of point-inversion symmetry, $\Phi(0) = F_d^+(0) = F_d^-(0)$ is the true friction force. Remarkably, the same symmetries, which rely here on our choice $\alpha = 1/2$ in Equation S46 of the two-state model, are observed in our experiments (Fig. S1). This observation suggests that the kinetics of the conformational change associated with gating of a transduction channel may result from thermal crossing of an energy barrier that is positioned nearly half way between the open and closed states of the channel along the axis of movement.

Section 5: **Physical description of active hair-bundle mechanics with finite activation kinetics of the transduction channels (with parameter Table S1)**

In this section, we modify a published description of active hair-bundle mechanics (21, 22) to account for the kinetics of transduction channels' gating. We compute the time-dependent external force

$$F(t) = \lambda_H \frac{d\bar{X}}{dt} + K_{GS}(\bar{X} - \bar{X}_a - D\,P_o) + K_{SP}\bar{X} \tag{S61}$$

to impose a symmetric triangular waveform of deflection $X(t) = \bar{X} - \bar{X}_S$ to the hair bundle. Deflection is measured with respect to the steady-state position $\bar{X}_S$ that the hair bundle assumes when $F = 0$. In response to the stimulus, adaptation motors display a movement $X_a(t) = \bar{X}_a(t) - \bar{X}_{a,S}$ with respect to their steady-state position $\bar{X}_{a,S}$. The position $\bar{X}_a(t)$ and the open probability $P_o(t)$ of the transduction channels vary with time according to:

$$\lambda_a \frac{d\bar{X}_a}{dt} = K_{GS}(\bar{X} - \bar{X}_a - D\,P_o) - K_{ES}\left(\bar{X}_a - \bar{X}_{a,S}\right) - F_{MAX}(1 - SP_o), \tag{S62}$$

$$\tau_c \frac{dP_o}{dt} = P_\infty - P_o \ . \tag{S63}$$

In Equations S61-S62, λ_H is the hydrodynamic drag coefficient of the hair bundle, λ_a is the slope of the force-velocity relation of the adaptation motors, K_{GS}, K_{SP}, and K_{ES} are elastic coefficients for the gating springs, the stereociliary pivots, and linkages that limit the extent of adaptation, respectively, D is the gating swing, F_{MAX} is the maximal force that adaptation motors produce at stall, and S is the strength of calcium-mediated feedback on the motor force. Without loss of generality, at steady state, we set the transduction channels' open probability $P_\infty^S = 0.5$ when $F = 0$. At this operating point, the steady-state positions of the hair bundle and of the adaptation motors are $\bar{X}_S = -(K_{GS}/K_{SP}) \times \left(\Delta G^{\emptyset}/Z\right)$, $\bar{X}_{a,S} = -\left\{D/2 + [1 + (K_{GS}/K_{SP})] \times \left(\Delta G^{\emptyset}/Z\right)\right\}$, respectively, and $F_{MAX} = \left(K_{GS} \times \Delta G^{\emptyset}\right)/[Z \times (1 - S/2)]$, in which $\Delta G^{\emptyset}$ is the intrinsic energy difference between open and closed states of the channels. In the presence of an external force $(F \neq 0)$, the open probability of transduction channels at steady state is given by

$$P_\infty = \{1 + \exp[-(X - X_a)/\delta]\}^{-1}, \quad \text{(S64)}$$

where $\delta = (k_B T)/(K_{GS} D/N)$, N is the number of transduction elements, and $k_B T$ is the thermal energy. Equation S63 accounts for the finite activation kinetics of the transduction channels (SI Appendix section 4). The characteristic timescale τ_c of channel activation depends on position and can be written as

$$\tau_c = 2\tau/[\exp(\alpha\,(X - X_a)/\delta) + \exp(-(1-\alpha)\,(X - X_a)/\delta)]\ , \quad \text{(S65)}$$

where $0 < \alpha < 1$ is the fractional distance of the transition state from the closed state and τ is the activation time for small deflections near an open probability of 1/2.

We considered three cases (see Fig. 4 in main text). Case I: the transduction machinery is fully functional (Fig. 4C and black solid line in Figs. 4E-F). In this case, we imposed a calcium-feedback strength S = 0.8 on the adaptation motor force (21-22). Case II: the channels can open and close but there is no adaptation (Figs. 4A-B and dotted lines in Figs. 4E-F). To describe the behavior of a passive hair bundle, we set $X_a = 0$ at all times. Our choice of the operating point $P_\infty^S = 0.5$ when there is no external force then yields $\bar{X}_S = 0$ and $\bar{X}_{a,S} = -D/2$. Case III: the adaptation motors can move but the transduction channels are blocked in an open state (Fig. 4D and red trace in Fig. 4E). Accordingly, we imposed in our simulations that there is no calcium feedback (S = 0) and that the channels' open probability is fixed at $P_O = 1$ at all times. At stady state, with $P_\infty^S = 0.5$, we then have $\bar{X}_{a,S} = -F_{MAX} \times (K_{SP} + K_{GS})/(K_{SP} \times K_{GS}) - D$ and $\bar{X}_S = -F_{MAX}/K_{SP}$. The two coupled Equations S62-S63 were integrated by the Euler method. Parameter values are listed in Table S1.

Table S1: Variables definition and parameter values.

All displacements and forces are expressed along the horizontal axis of a bundle's vertical plane of bilateral symmetry that contains the point of application of the external force. Note that because bundle movements are transmitted to the transduction apparatus via oblique tip links, there is a geometrical projection factor $\gamma = 0.14$ (8, 19) between the gating-spring extension x and the bundle deflection X: $x = \gamma\, X$. Similarly, a change in gating-spring tension Δt_{GS} creates an horizontal force on the hair bundle given by $\gamma\ \Delta t_{GS}$.

Variable	Definition	Relation to other variables	Value
P_{∞}^{S}	Channel open probability at steady state with no external force		0.5
N	Number of transduction elements		50
D (nm)	Reduction of gating-spring extension upon channel opening		50
α	Fractional distance to the transition state		0.5
$\Delta G^{\emptyset}$ (zJ)	Intrinsic energy difference between open and closed states of the channels		40
τ (µs)	Channel activation time near an open probability of 0.5		500
λ_H (µN·s/m)	Hydrodynamic drag coefficient of the hair bundle		0.1
K_{GS} (mN/m)	Combined stiffness of the gating springs		0.8
K_{SP} (mN/m)	Combined stiffness of the stereociliary pivots		0.2
K_{∞} (mN/m)	Hair-bundle stiffness with $P_o = 0$ or 1	$K_{\infty} = K_{GS} + K_{SP}$	1
Z (pN)	Reduction of tip-link tension upon channel opening	$Z = K_{GS}\, D/N$	0.8
$k_B T$ (zJ)	Thermal energy		4
δ (nm)	Characteristic lengthscale of mechano-sensitivity	$\delta = (k_B T)/Z$	5
λ_a (µN·s/m)	Slope of the force-velocity relation of the adaptation motor		10
F_{MAX} (pN)	Maximal force that the adaptation motor produces at stall	$\dfrac{K_{GS} \times \Delta G^{\emptyset}}{Z \times (1 - S/2)}$	66.67
S	Ca^{2+}-feedback strength		0.8 or 0
K_{ES} (mN/m)	Combined stiffness of extent springs		1.6

SUPPLEMENTARY REFERENCES

1. Feyman RP, Leighton RB, Sands M (1964) *The Feynman Lectures on Physics. Vol. II* (Addison-Wesley, Reading, MA).
2. Landau LD, Lifshitz EM (1986) *Theory of elasticity* (Pergamon Press, Oxford) 3rd edition Ed p 180.
3. Gittes F, Mickey B, Nettleton J, Howard J (1993) Flexural rigidity of microtubules and actin filaments measured from thermal fluctuations in shape. *J Cell Biol* 120(4):923-934.
4. Howard J (2001) *Mechanics of Motor Proteins and the Cytoskeleton* (Sinauer Associates, Sunderland, MA).
5. Wiggins CH, Riveline D, Ott A, Goldstein RE (1998) Trapping and wiggling: elastohydrodynamics of driven microfilaments. *Biophys J* 74(2 Pt 1):1043-1060.
6. Martin P, Hudspeth AJ, Jülicher F (2001) Comparison of a hair bundle's spontaneous oscillations with its response to mechanical stimulation reveals the underlying active process. *Proc Natl Acad Sci USA* 98(25):14380-14385.
7. Martin P, Hudspeth AJ (1999) Active hair-bundle movements can amplify a hair cell's response to oscillatory mechanical stimuli. *Proc Natl Acad Sci USA* 96(25):14306-14311.
8. Howard J, Hudspeth AJ (1988) Compliance of the hair bundle associated with gating of mechanoelectrical transduction channels in the bullfrog's saccular hair cell. *Neuron* 1(3):189-199.
9. Meyhofer E, Howard J (1995) The force generated by a single kinesin molecule against an elastic load. *Proc Natl Acad Sci USA* 92(2):574-578.
10. Kozlov AS, Risler T, Hudspeth AJ (2007) Coherent motion of stereocilia assures the concerted gating of hair-cell transduction channels. *Nat Neurosci* 10(1):87-92.
11. Corey DP, Hudspeth AJ (1983) Kinetics of the receptor current in bullfrog saccular hair cells. *J Neurosci* 3(5):962-976.
12. Markin VS, Hudspeth AJ (1995) Gating-spring models of mechanoelectrical transduction by hair cells of the internal ear. *Annu Rev Biophys Biomol Struct* 24:59-83.
13. Ricci AJ, Kennedy HJ, Crawford AC, Fettiplace R (2005) The transduction channel filter in auditory hair cells. *J Neurosci* 25(34):7831-7839.
14. Martin P, Mehta AD, Hudspeth AJ (2000) Negative hair-bundle stiffness betrays a mechanism for mechanical amplification by the hair cell. *Proc Natl Acad Sci USA* 97(22):12026-12031.
15. Kozlov AS, Baumgart J, Risler T, Versteegh CP, Hudspeth AJ (2011) Forces between clustered stereocilia minimize friction in the ear on a subnanometre scale. *Nature* 474(7351):376-379.
16. Martin P, Hudspeth AJ (2001) Compressive nonlinearity in the hair bundle's active response to mechanical stimulation. *Proc Natl Acad Sci USA* 98(25):14386-14391.
17. Lim DJ (1986) Functional structure of the organ of Corti: a review. *Hear Res* 22(1-3):117-146.
18. Nam JH, Fettiplace R (2008) Theoretical conditions for high-frequency hair bundle oscillations in auditory hair cells. *Biophys J* 95(10):4948-4962.
19. Jacobs RA, Hudspeth AJ (1990) Ultrastructural correlates of mechanoelectrical transduction in hair cells of the bullfrog's internal ear. *Cold Spring Harb Symp Quant Biol* 55:547-561.
20. Kennedy HJ, Evans MG, Crawford AC, Fettiplace R (2003) Fast adaptation of mechanoelectrical transducer channels in mammalian cochlear hair cells. *Nat Neurosci* 6(8):832-836.
21. Tinevez JY, Jülicher F, Martin P (2007) Unifying the various incarnations of active hair-bundle motility by the vertebrate hair cell. *Biophys J* 93(11):4053-4067.
22. Nadrowski B, Martin P, Jülicher F (2004) Active hair-bundle motility harnesses noise to operate near an optimum of mechanosensitivity. *Proc Natl Acad Sci USA* 101(33):12195-12200.